

Accepted for publication in the Astrophysical Journal

Amplification, Saturation, and Q Thresholds for Runaway: Growth of Self-Gravitating Structures in Models of Magnetized Galactic Gas Disks

Woong-Tae Kim and Eve C. Ostriker

*Department of Astronomy, University of Maryland
College Park, MD 20742-2421*

kimwt@astro.umd.edu, ostriker@astro.umd.edu

ABSTRACT

We investigate the susceptibility of gaseous, magnetized galactic disks to formation of self-gravitating condensations using two-dimensional, local models. We focus on two issues: (1) determining the threshold condition for gravitational runaway, taking into account nonlinear effects, and (2) distinguishing the magneto-Jeans instability (MJI) that arises under inner-galaxy rotation curves from the modified swing amplification (MSA) that arises under outer-galaxy rotation curves. For axisymmetric density fluctuations, instability is known to require a Toomre parameter $Q < 1$. For nonaxisymmetric fluctuations, any nonzero shear $q \equiv -d \ln \Omega / d \ln R$ winds up wavefronts such that in linear theory amplification saturates. Any Q threshold for nonaxisymmetric gravitational runaway must originate from nonlinear effects. We use numerical magnetohydrodynamic simulations to demonstrate the anticipated threshold phenomenon, to analyze the nonlinear processes involved, and to evaluate the critical value Q_c for stabilization. We find $Q_c \sim 1.2 - 1.4$ for a wide variety of conditions, with the largest values corresponding to nonzero but subthermal mean magnetic fields. Our findings for Q_c are similar to those inferred from thresholds for active star formation in the outer regions of spiral galaxies. MJI is distinct from MSA in that opposition to Coriolis forces by magnetic tension, rather than cooperation of epicyclic motion with kinematic shear, enables nonaxisymmetric density perturbations to grow. We suggest that under low-shear inner-disk conditions, Q_c will be larger than that in outer disks by a factor $\sim (v_A/qc_s)^{1/2}$, where v_A and c_s are the respective Alfvén and sound speeds.

Subject headings: galaxies: ISM — galaxies: kinematics and dynamics — galaxies: structure — instabilities — ISM: kinematics and dynamics — ISM: magnetic fields — MHD — stars: formation

1. Introduction

1.1. Observational motivation and previous theory

In the Milky Way and external spiral galaxies, most of the molecular gas is found in cold, giant molecular clouds (GMCs) within which most of star formation takes place (e.g., Young & Scoville (1991); Williams, Blitz, & McKee (2000)). Star forming GMCs are strongly associated with spiral arms (e.g., Stark (1979); Solomon et al (1985); Kenney (1997)), and often tend to appear in clusters, forming giant molecular associations (GMAs) (e.g., Cohen et al (1985); Grabelsky et al (1987); Vogel et al (1988); Rand & Kulkarni (1990); Rand (1993); Sakamoto et al (1999)). GMAs are present even in flocculent galaxies where spiral arms are relatively weak (Sakamoto 1996; Thornley & Mundy 1997a,b). Recent studies of internal structure and dynamics have significantly improved our understanding of GMCs and GMAs; but their formation mechanisms remain subject to considerable uncertainty.

A suggestion of long standing is that GMCs or GMAs form through gravitational instabilities either in galactic disks at large or within spiral arms (Goldreich & Lynden-Bell (1965); Lynden-Bell (1966); Elmegreen (1979, 1987a, 1994); Elmegreen & Elmegreen (1983); Balbus & Cowie (1985); Balbus (1988); Gammie (1992, 1996), see also reviews in Elmegreen (1993a, 1995a, 1996) and references therein). Goldreich & Lynden-Bell (1965, hereafter GLB) used a linear-theory analysis to show that nonaxisymmetric perturbations may grow strongly in a shearing disk, provided self-gravity is sufficient. Amplification of a linear disturbance is ultimately limited by differential rotation, which shears any wavelet into a tightly-wrapped trailing spiral pattern in which (stabilizing) pressure overmasters (destabilizing) self-gravity. This mechanism for transient growth of perturbations in both the gaseous disks of GLB and their stellar counterparts (Julian & Toomre 1966, hereafter JT) has come to be called a “swing amplifier” (Toomre 1981).

Operating on a large scale in a galactic disk, swing amplification may potentially lead to the formation of self-gravitating cloud complexes with sizes and masses set by the two-dimensional (2D) Jeans scale (Elmegreen & Elmegreen 1983; Elmegreen 1987a). The characteristic Jeans-unstable scale of ~ 1 kpc and mass of $\sim 10^7 M_\odot$ (see §2.2) appear to be in good agreement with observed HI superclouds (Elmegreen & Elmegreen 1983; Elmegreen 1987b; Knapen et al 1993) or GMAs (Rand 1993; Sakamoto 1996; Thornley & Mundy 1997a,b; Sakamoto et al 1999). Gravitational instabilities may also operate on a smaller scale within a pre-existing spiral arm (Balbus & Cowie 1985; Balbus 1988; Elmegreen 1994). In particular, Balbus & Cowie (1985) and Balbus (1988) showed that the density enhancement and shear profile inside a spiral wave crest can trigger near-axisymmetric and swing-like gravitational instabilities that could develop into cloud complexes with masses and spacings consistent with observations. The presence of spiral arms may not be necessary for cloud formation via instabilities, but the ambient high-density, low-shear conditions within arms are generally more favorable for Jeans-type instabilities than conditions in interarm regions (Elmegreen 1994).

Effects of magnetic fields on linear gravitational instabilities in 2D differentially-rotating disks have been thoroughly investigated by Elmegreen (1987a, 1994), Gammie (1996) and Fan & Lou (1997). These studies extended the works of Chandrasekhar (1954) and Lynden-Bell (1966) for gravitational instability in a magnetized, uniformly-rotating disk to incorporate the effects of shear analyzed by GLB. In regions of disks with weak shear, magnetic field tension enhances instability by redistributing angular momentum (breaking the conserved-potential vorticity constraint), while in strongly-shearing regions the magnetic field pressure combines with thermal pressure (and the Coriolis force) in tending to suppress linear instabilities.

Formation of molecular clouds via large-scale gravitational instability also, implicitly, underlies the proposal that global star formation in disk galaxies is regulated by the value of the Toomre Q parameter (for the definition of Q see eq. [7] below). Following the pioneering work of Quirk (1972), who suggested a threshold model for star formation, Kennicutt (1989) found that active star formation requires azimuthally-averaged gas surface density corresponding to $Q \lesssim Q_c = 1.6$ for massive spirals¹ (also see the review of Kennicutt (1997) and references therein). This azimuthally averaged Q threshold model appears successfully to explain the radial distributions of star formation rates and gas surface densities also in low surface brightness spirals (van der Hulst et al 1993) and HII galaxies (Taylor et al 1994). Rand (1993) studied the azimuthal variation of surface density in the grand-design spiral M51 and found that the ratio of actual to critical surface densities is higher in the arms than in the interarm regions, indicating that arm gas is more prone to the gravitational instabilities.

While models that appeal to a threshold in the Toomre Q parameter as a star formation criterion are operationally quite successful in identifying observed outer radii for active star formation in spiral galaxies, the theoretical underpinning of the threshold concept is indirect. In particular, the literature has lacked an explicit theoretical demonstration and evaluation of thresholds for generic (*nonaxisymmetric*) gravitational runaways. The star formation threshold concept, by utilizing an azimuthally-averaged surface density, borrows its physical grounds from the *axisymmetric* instability of Safronov (1960) and Toomre (1964). Axisymmetric (ring-like) instability in a thin gas disk requires $Q < 1$ (Lin & Shu (1971); see e.g., Shu (1992)), which is generally not realized in galaxies. Kennicutt (1989) attributed the fact of the apparent critical Q_c exceeding unity to the results of two-fluid (star+gas) instabilities (Jog & Solomon 1984a,b), with the stellar disk’s self-gravity enhancing instability and hence raising Q_c . The stabilizing effect from pervasive magnetic fields to axisymmetric perturbations, which would tend to decrease Q_c , must however be considered as well (Elmegreen 1992).

In the more general, *nonaxisymmetric* case, perturbations experience significant amplification as they swing from leading to trailing (GLB; JT; Toomre (1981)) for a range of Q both greater and smaller than unity. Because the magnitude of swing amplification is continuous with respect

¹The enhanced study of Martin & Kennicutt (2001), contemporary with the present work, reports a mean observational threshold for active star formation at $Q_c = 1.4$.

to Q in the linear theory, those analyses cannot establish a decisive critical value for Q . Elmegreen (1991, 1994) suggested that parallel secondary instabilities in either shearing wavelets that have grown from swing amplification, or in spiral density waves, have effective thresholds $Q_c \sim 1 - 2$. But this suggestion needs to be confirmed by numerical simulations, because the background state for onset of parallel instabilities is not in the linear regime.

Although the linear gravitational instability analyses are useful and effective in predicting approximate sizes, spacings, and formation time scales of giant cloud complexes, as well as approximate star formation threshold densities and radii, the linear theory still has to be supplemented by nonlinear simulations. This is because the instability in either general disk planes or spiral arms shows only transient growth, eventually stabilized by the kinematic increase of the local wavenumber due to background shear (e.g., Elmegreen (1987a)) or by expansion of the background flow off the arms (Balbus & Cowie 1985). The transient nature of local gravitational instabilities allows only limited time for perturbations to grow. The evolution of a system subject to a transient instability depends on the initial perturbation amplitude; if the initial perturbation level is too low, the system may never reach a nonlinear phase. This is unlike a true instability, in which disturbances grow exponentially until nonlinear saturation occurs, regardless of their initial amplitudes. The amplification factor in shear instability is a sensitive function of wavenumbers, and mode coupling is inevitable in the nonlinear stage of evolution. Numerical simulations with realistic power spectra as well as realistic initial amplitudes for perturbations are thus crucial for fully and quantitatively understanding the significance of gravitational instability in the formation of giant cloud complexes and regulation of global star formation.

1.2. Program for this work

In this paper, we investigate both linear and nonlinear evolution of large scale gravitational instabilities in magnetized, shearing disks by solving the ideal magnetohydrodynamics (MHD) equations, and we study the implications of these models for the formation of gravitationally bound cloud complexes. We consider a local patch of an infinitesimally thin gaseous galactic disk with physical conditions similar to the solar neighborhood or other outer-galaxy regions. We also consider models with reduced rotational shear, representing inner-galaxy conditions. Initially, uniform magnetic fields in the azimuthal direction are included, and we adopt either an isothermal or an adiabatic equation of state. We do not include background spiral arm potentials in the present study, focusing solely on the development of local instabilities and their nonlinear outcomes in a featureless gravitational potential. Although direct application of our results can be made, for example, to interarm regions or to flocculent galaxies where spiral arms are absent or weak, extrapolation of our results with parameters suitable for the interiors of spiral arms may yield insight on formation of clouds in spiral galaxies with strong arms. Effects of spiral arm potentials will be explicitly considered in a subsequent paper. Related numerical work has been reported very recently by Gammie (2001), who studied (without magnetic fields) the effect of cooling on gravita-

tional instability and transport of angular momentum by gravitational torques, for application to accretion disks around young stellar objects or active galactic nuclei.

Our primary objectives in this paper are to understand the nonlinear evolution of gravitational instabilities in disks, and to find the range of Q in high-shear regions that permits the ultimate formation of gravitationally bound objects. We also perform a linear analysis with particular emphasis on the dependence of gravitational instability upon shear rate and field strength, to investigate how inner- and outer- galaxy instabilities may differ. The linear time evolution of the system we are exploring was previously studied by Elmegreen (1987a) and Fan & Lou (1997) (see also Gammie (1996)), who integrated time-dependent, shearing-sheet equations directly, treating the nonaxisymmetric instability as an initial-value problem (GLB; JT). We follow the same “shearing-sheet” approach to elucidate the distinction between two separate instabilities that occur: magneto-Jeans instability (MJI) when shear is weak and/or the magnetic field is very strong; and magnetically modified swing amplification (MSA) when shear is relatively strong and magnetic fields are moderate or weak. Because the shear rate varies with radius, we expect the MJI and MSA to be important, respectively, in inner and outer galaxies (modulo the effects of spiral arms). MJI and MSA are generalizations, respectively, of the dynamical processes first studied by Lynden-Bell (1966) and by GLB. By seeking coherent wavelet solutions, we obtain an algebraic dispersion relation for magneto-Jeans modes.

Our treatment of gaseous disks as perfectly-conducting, adiabatic or isothermal monolayers admittedly idealizes the complex, multiphase interstellar medium (ISM) in real galaxies. Because we study growth of structure in near-uniform media with small perturbations, our models are also idealized in that we consider what would happen to a disk if it were born in, or evolved to, a state of near homogeneity. Physically, this initial state could be directly achieved by the cooling down of a disk that starts hot or has been heated sufficiently that all large-amplitude perturbations are smoothed out by pressure forces. Perhaps more practically, our models also apply to observable galaxies to the extent that their coherent over-density perturbations on radial scales of $\sim 3 - 5$ kpc are not large; as we shall show, smaller-scale perturbations, although they may initially have significant amplitude, do not grow strongly. As we shall also show, nonlinear interactions of small-scale but moderate-amplitude perturbations may produce larger-scale low-amplitude perturbations, which are then susceptible to gravitational runaway if Q is sufficiently small. In our simulations, we describe this phenomenon as the “rejuvenated swing” secondary instability; but for real galaxies this might be the most common way in which gravitationally-bound clouds could grow outside of spiral arms.

The organization of this paper is as follows. In the next section, we present the vertically integrated, 2D MHD equations, and describe the characterization of our models via physical and dimensionless parameters. In §3, we revisit previous linear analysis to provide coherent wavelet dispersion relations and compute total amplification magnitudes, and thus to distinguish magneto-Jeans modes from magnetically modified swing amplifications. We then turn to nonlinear investigations using numerical MHD methods. The computational code we use and the test results for

the code performance are described in §4. In §5 and §6, respectively, we present the results of local disk simulations with weakly- and strongly-shearing background flows. These represent nonlinear evolution of the MJI and MSA regimes, respectively. We analyze the dependence of our results on a variety of input parameters, in particular focusing on what may determine the threshold for collapse, and what routes the collapse may follow. We summarize our results and discuss the astronomical implications of our work in §7.

The reader interested primarily in our quantitative findings for the separate gravitational runaway threshold criteria that apply under weak shear (inner galaxy) and strong shear (outer galaxy) conditions may wish to omit the technical sections 2-6 and turn directly to §7.

2. Basic equations and model parameters

2.1. Two dimensional magnetohydrodynamic equations

In this paper we study both linear and nonlinear instabilities of galactic disks employing a local, thin-disk approximation. We consider a patch of the disk whose center lies at a distance R_0 from the galactic center and rotates with a constant angular velocity $\Omega(R_0)$ about the galactic center, and work in a local Cartesian reference frame with x and y representing the radial and the azimuthal directions, respectively (GLB; JT). We expand the compressible, ideal MHD equations in the local frame, and neglect terms arising from the curvilinear geometry. The equilibrium profile of angular velocity in the background flow relative to the center of the box at $x = y = 0$ is then expressed by $\mathbf{v}_0 \equiv -q\Omega x \hat{\mathbf{y}}$, where $q \equiv -d \ln \Omega / d \ln R$ measures the shear. We finally integrate the resulting equations in the vertical direction to obtain the following set of 2D equations:

$$\frac{\partial \Sigma}{\partial t} + \nabla \cdot (\Sigma \mathbf{v}) = 0, \quad (1)$$

$$\frac{\partial \mathbf{v}}{\partial t} + \mathbf{v} \cdot \nabla \mathbf{v} = -\frac{1}{\Sigma} \nabla \Pi + \frac{1}{4\pi \Sigma} (\nabla \times \mathbf{B}) \times \mathbf{B} + 2q\Omega^2 x \hat{\mathbf{x}} - 2\boldsymbol{\Omega} \times \mathbf{v} - \nabla \Phi, \quad (2)$$

$$\frac{\partial U}{\partial t} + \nabla \cdot (U \mathbf{v}) = -\Pi \nabla \cdot \mathbf{v}, \quad (3)$$

$$\frac{\partial \mathbf{B}}{\partial t} = \nabla \times (\mathbf{v} \times \mathbf{B}), \quad (4)$$

and

$$\nabla^2 \Phi = 4\pi G \Sigma \delta(z), \quad (5)$$

(cf, Hawley, Gammie, & Balbus (1995); Gammie (2001)). Here, Σ is the surface density, \mathbf{v} is the vertically-averaged velocity, Π and U are the 2D vertically-integrated pressure and internal energy, Φ is the self-gravitational potential, and \mathbf{B} is the midplane value of the 3D magnetic field times the square root of the unperturbed ratio of surface density to midplane volume density. In equations

(2) and (4), we treat the effective scale height of the magnetic field as a constant in space and time.² In equation (5), G and δ are the gravitational constant and the Kronecker delta, respectively.

As expressed by equation (3), in this paper we do not include thermal heating and cooling effects other than those due to the volumetric change (including shocks). We assume an ideal gas equation of state

$$\Pi = (\gamma - 1)U, \quad (6)$$

where γ is the 2D adiabatic index which differs from a 3D adiabatic index γ_a . With $\mathbf{B} = 0$, in the low frequency limit, $\gamma = (3\gamma_a - 1)/(\gamma_a + 1)$ (Ostriker, Shu, & Adams 1992), while $\gamma = 3 - 2/\gamma_a$ for a strongly self-gravitating disk (Gammie 2001). In an isothermal medium, $\gamma = \gamma_a = 1$. When B_{3D}^2/ρ is vertically constant and self-gravity is not strong, the presence of magnetic pressure yields $\gamma = (3\gamma_a - 1 + (2\gamma_a + 1)/2\beta)/(\gamma_a + 1 + 3/2\beta)$ for axisymmetric modes. In most of simulations presented in this paper, we adopt $\gamma = 1.5$, corresponding to $\gamma_a = 5/3$ for unmagnetized low-frequency perturbations (for axisymmetric modes with $\gamma_a = 5/3$ and $\beta = 1$ or 10, $\gamma = 1.48$ or 1.50, respectively). As we shall show later, however, instability criteria turn out to be rather insensitive to the particular choice of γ .

2.2. Model parameters

We consider as an unperturbed initial equilibrium state a homogeneous medium having uniform surface density Σ_0 , uniform azimuthal magnetic fields $\mathbf{B}_0 = B_0\hat{\mathbf{y}}$, thermal sound speed $c_s \equiv (\gamma\Pi_0/\Sigma_0)^{1/2}$, and shear velocity profile \mathbf{v}_0 . We follow the dynamical evolution of a square domain of size L . The fundamental dimensional units for length, time, and mass are the box edge L , the rotation time Ω^{-1} of the background flow, and the total mass $M_{\text{tot}} = L^2\Sigma_0$ contained in the box. The natural scaling for the other variables is $L\Omega$ for \mathbf{v} , $L^2\Omega^2\Sigma_0$ for Π and U , $L\Omega(4\pi\Sigma_0)^{1/2}$ for \mathbf{B} , and $L^2\Omega^2$ for Φ . The governing equations (1)-(6) in dimensionless form then depend only on the dimensionless gravitational constant $g \equiv G\Sigma_0/L\Omega^2$. In terms of these non-dimensional variables, the initial equilibrium is represented by $\Sigma = 1$, $\mathbf{v} = -qx\hat{\mathbf{y}}$, $U = a^2/(\gamma(\gamma - 1))$, and $\mathbf{B} = a\beta^{-1/2}\hat{\mathbf{y}}$, where the dimensionless sound speed a and the dimensionless plasma parameter β are defined respectively by $a \equiv c_s/L\Omega$ and $\beta \equiv c_s^2/v_A^2$ along with the Alfvén speed $v_A^2 \equiv B_0^2/4\pi\Sigma_0 \equiv B_{0,3D}^2/4\pi\rho_0$. Therefore, the specification of a , g , and β would (together with q and γ) completely describe the initial unperturbed configuration of a model disk.

Instead of using a and g directly, we employ two input parameters that are equivalent to a and

²Strictly speaking, the scale height would vary in response to thermal pressure and magnetic pressure and tension variations. Our simplified treatment neglects force terms arising from the compression and dilution of magnetic fields by this vertical contraction/expansion, and also neglects vertical magnetic tension force terms that would arise from scale height variations along a given field line. A full 3D treatment that allowed for these terms would permit a study of the coupling between the Parker instability and MJI/MSA; here, by neglecting magnetic scale height variations we focus exclusively on the isolating the effects of the latter.

g but more illuminating in the context of galactic dynamics. One is Toomre’s parameter (modified for a razor-thin gaseous disk)

$$Q \equiv \frac{\kappa c_s}{\pi G \Sigma_0} = \frac{a}{\pi g} \sqrt{4 - 2q}, \quad (7)$$

where κ stands for the epicycle frequency, $\kappa^2 \equiv R^{-3} d(R^4 \Omega^2)/dR$. The other is the Jeans number

$$n_J \equiv \frac{G \Sigma_0 L}{c_s^2} = \frac{g}{a^2}, \quad (8)$$

of a patch of a 2D thin disk. For given values of c_s and κ , the Q parameter measures the surface density relative to the threshold value at $Q = 1$ for axisymmetric gravitational instabilities (Toomre (1964); see e.g., Binney & Tremaine (1987); Shu (1992)), while n_J is the ratio of the simulation box size L to the shortest wavelength $\lambda_J \equiv c_s^2/G\Sigma_0$ permitting gravitational instability in a thin (nonrotating) disk. We may define the 2D Jeans mass M_J via n_J as $M_J \equiv M_{\text{tot}}/n_J^2 = c_s^4/G^2\Sigma_0$.

Our initial disks are smoothed versions of galactic gaseous components, so it is useful to show how our dimensionless simulation variables relate to the large-scale dimensional properties of the Milky Way’s ISM. The atomic plus molecular disks inside the solar circle together contribute $7 - 15 \text{ M}_\odot \text{ pc}^{-2}$ (allowing for He) to the surface density (Dame 1993). In the solar neighborhood, the warm components contribute a total surface density $\sim 6 \text{ M}_\odot \text{ pc}^{-2}$ (Kulkarni & Heiles 1987), so that the total solar-neighborhood value is $\sim 13 \text{ M}_\odot \text{ pc}^{-2}$. In the solar neighborhood, the epicyclic frequency is $\kappa = 36 \text{ km s}^{-1} \text{ kpc}^{-1}$ (Binney & Tremaine 1987), and for a near-flat rotation curve (corresponding to $q \approx 1$) $\kappa \propto R^{-1}$. Many uncertainties surround both the theoretical concept and observational measures of a “mean” thermal pressure, but a number of arguments support a consistent picture with $P/k \sim 2000 - 4000 \text{ K cm}^{-3}$ (Heiles 2000). With mean midplane density $\sim 0.6 \text{ cm}^{-3}$ (Dickey & Lockman 1990), this implies a sound speed $c_s = 6 - 8 \text{ km s}^{-1}$. With a mean 3D magnetic field strength $B_{0,3D} = 1.4 \mu \text{ G}$ (Rand & Lyne 1994), the implied Alfvén speed is $v_A = 3.1 \text{ km s}^{-1} (B_{0,3D}/1.4 \mu \text{ G})(n_H/1 \text{ cm}^{-3})^{-1/2}$. We write our dimensionless simulation parameters relative to dimensional ISM values as

$$Q = 1.4 \left(\frac{c_s}{7.0 \text{ km s}^{-1}} \right) \left(\frac{\kappa}{36 \text{ km s}^{-1} \text{ kpc}^{-1}} \right) \left(\frac{\Sigma_0}{13 \text{ M}_\odot \text{ pc}^{-2}} \right)^{-1}, \quad (9)$$

$$L = n_J \times 0.87 \text{ kpc} \left(\frac{c_s}{7.0 \text{ km s}^{-1}} \right)^2 \left(\frac{\Sigma_0}{13 \text{ M}_\odot \text{ pc}^{-2}} \right)^{-1}, \quad (10)$$

$$\beta = 6 \left(\frac{P/k}{3000 \text{ K cm}^{-3}} \right) \left(\frac{B_{0,3D}}{1.4 \mu \text{ G}} \right)^{-2}, \quad (11)$$

for $\gamma_a = 5/3$, with the 2D Jeans mass $\Sigma_0 \lambda_J^2$ given by

$$M_J = 10^7 \text{ M}_\odot \left(\frac{c_s}{7.0 \text{ km s}^{-1}} \right)^4 \left(\frac{\Sigma_0}{13 \text{ M}_\odot \text{ pc}^{-2}} \right)^{-1}. \quad (12)$$

From equations (9)-(12), therefore, we can see that with solar-neighborhood values, our model disk patch with $n_J = 5$ corresponding to $L = 4.4 \text{ kpc}$ contains about $2.5 \times 10^8 \text{ M}_\odot$ and is locally stable to axisymmetric instabilities.

Before finishing this section, we remark on a few dynamical time scales of note. They are the rotation time that we choose as the time unit in our simulations, $t_r \equiv 1/\Omega = 3.8 \times 10^7 \text{ yrs} (\Omega/26 \text{ km s}^{-1} \text{ kpc}^{-1})^{-1}$, corresponding to the orbital period,

$$t_{\text{orb}} \equiv 2\pi t_r = \frac{2\pi}{\Omega} = 2.4 \times 10^8 \text{ yrs} \left(\frac{\Omega}{26 \text{ km s}^{-1} \text{ kpc}^{-1}} \right)^{-1}, \quad (13)$$

the sound crossing time

$$t_s \equiv \frac{L}{c_s} = 6.3 \times 10^8 \text{ yrs} \left(\frac{L}{4.3 \text{ kpc}} \right) \left(\frac{c_s}{7 \text{ km s}^{-1}} \right)^{-1}, \quad (14)$$

and a characteristic gravitational contraction time

$$t_g \equiv \frac{t_s}{n_J} = \frac{c_s}{G\Sigma_0} = 1.2 \times 10^8 \text{ yrs} \left(\frac{c_s}{7 \text{ km s}^{-1}} \right) \left(\frac{\Sigma_0}{13 \text{ M}_\odot \text{ pc}^{-2}} \right)^{-1}. \quad (15)$$

The growth rate for the fastest-growing ($\lambda = \lambda_J/2$) gravitationally-unstable mode in a nonrotating disk is πt_g^{-1} . The shearing time, corresponding to the time for points on opposite sides of the box to separate by distance L in azimuth, is $t_{sh} \equiv 1/q\Omega$, which equals t_r for a disk with a flat rotation curve ($q = 1$). The small value of t_{sh} compared with t_s and t_g shows that incorporation of galactic differential rotation is essential in the study of the dynamical evolution of the ISM on a large scale.

3. Linear analysis

Although the linear theory for gravitational instability in disks with shearing background flows can be found in GLB for an unmagnetized system, and in Elmegreen (1987a, 1994), Gammie (1996), and Fan & Lou (1997) for a magnetized system, we revisit it with particular attention to the dependence of the instability on the shear parameter q and on the plasma parameter β . Our objectives in this section are to obtain an algebraic dispersion relation for the instability in the limit of weak shear or strong magnetic fields (MJI), and to distinguish it from the strong-shear instability with relatively weak magnetic fields (MSA).

3.1. Linearized equations

We begin by considering a thin self-gravitating gaseous disk with differential rotation, and initially uniform surface density and uniform azimuthal magnetic fields. We adopt a local approximation to investigate the behavior of disturbances whose wavelengths are small compared with the size of the Galaxy, using the governing set of equations (1)-(6). The stability of a local patch of the disk can be studied in the shearing sheet coordinates $(x', y', t') = (x, y + q\Omega x t, t)$ (GLB; JT). We consider the time development of an initial plane-wave disturbance which preserves sinusoidal variations in the local rest frame of the equilibrium shearing, rotating flow, i.e.

$$\chi_1(x', y', t') = \chi_1(t') \exp(ik_x x' + ik_y y'), \quad (16)$$

where χ_1 refers to any perturbed physical variable and k_x and k_y represent the initial respective wavenumbers along the $\hat{\mathbf{x}}$ - and $\hat{\mathbf{y}}$ -directions. We linearize the MHD equations (1)-(6) and apply perturbations of the form (16) in the transformed coordinates. The resulting equations can be written (omitting the prime on t)

$$\frac{d\sigma}{dt} = -k_x(t)u_x - k_y u_y, \quad (17)$$

$$\frac{du_x}{dt} = 2\Omega u_y + k_x(t) \left(c_s^2 - \frac{2\pi G \Sigma_0}{|k(t)|} \right) \sigma - v_A^2 k(t)^2 m, \quad (18)$$

$$\frac{du_y}{dt} = -\frac{\kappa^2}{2\Omega} u_x + k_y \left(c_s^2 - \frac{2\pi G \Sigma_0}{|k(t)|} \right) \sigma, \quad (19)$$

$$\frac{dm}{dt} = u_x. \quad (20)$$

Here, $\sigma \equiv \Sigma_1/\Sigma_0$, $\mathbf{u} \equiv i\mathbf{v}_1$, the dimensionless vector potential m is defined through $\mathbf{B}_1 \equiv -iB_0 \nabla \times (m\hat{\mathbf{z}})$, the time dependent wavenumber $k_x(t) \equiv k_x + q\Omega k_y t$, and $k(t)^2 \equiv k_x(t)^2 + k_y^2$.

Equations (17)-(20) are ordinary differential equations in time and the explicit time-dependence of $k(t)$ does not permit eigensolutions in general. This is the characteristic of any system with background shear. An applied spatial planform is wrapped up from leading to trailing configuration by the kinematics of shear; its radial wavenumber increases linearly with time. The response of the system to nonaxisymmetric disturbances can be studied through direct numerical integrations of the linearized equations as an initial value problem. Elmegreen (1987a) followed this approach to investigate nonaxisymmetric gravitational instabilities in the magnetized gaseous galactic disk as a supercloud formation mechanism. Gammie (1996) computed the nonaxisymmetric responsiveness of a magnetized disk under large differential rotation to gravitational instabilities, and showed that magnetic fields reduce the responsiveness. Fan & Lou (1997) extended Elmegreen’s work to study the long-term evolution of MHD density waves. We refer the reader to these works for illustrative examples of perturbed density evolutions.

3.2. Coherent wavelet analysis

While the general response of the system to nonaxisymmetric perturbations is found from the temporal integrations of equations (17)-(20), there are certain regimes in the parameter space in which we can seek time-localized “coherent wavelet” solutions having the same time dependence for all perturbed variables. The condition for the existence of the coherent solutions is that the time over which the instantaneous growth rate

$$\zeta(t) \equiv \frac{d \ln \chi_1(t)}{dt}, \quad (21)$$

changes is sufficiently large compared with the growth time ζ^{-1} , that is,

$$\left| \frac{d \ln \zeta(t)}{dt} \right| \ll \zeta(t) \quad (22)$$

(Kim & Ostriker 2000). This amounts to a temporal WKB limit. Since equation (22) can be written as $(q\Omega/\zeta)(k_x(t)k_y/k^2)(d\ln\zeta/d\ln k) \ll 1$, the existence of coherent wavelet solutions is guaranteed if shear is weak ($q\Omega \ll \zeta$), if the instantaneous growth rate is insensitive to k ($d\ln\zeta/d\ln k \ll 1$), or if modes are near-axisymmetric ($k_x(t)k_y/k^2 \ll 1$). This technique has been applied to study the effect of differential rotation on the Parker instability in the Galactic disk (Shu 1974) and on the convective instability in accretion disks (Ryu & Goodman 1992). Very recently Kim & Ostriker (2000) derived an analytic dispersion relation for nonaxisymmetric magnetorotational instabilities via the coherent wavelet formalism in a strong shear environment.

The coherent wavelet solutions for magneto-Jeans instabilities are immediately obtained by substituting equation (21) into equations (17)-(20) and then putting $d\chi_1/dt \rightarrow \zeta\chi_1$ following the approximation (22). The nontrivial solutions of the resulting equations obey a quadratic equation in ζ^2 :

$$\zeta^4 + [\kappa^2 - 2\pi G\Sigma_0|k| + (c_s^2 + v_A^2)k^2]\zeta^2 + [c_s^2k^2 - 2\pi G\Sigma_0|k|]v_A^2k_y^2 = 0. \quad (23)$$

Note that the time-dependence of ζ is absorbed implicitly in $k = k(t)$. It can be shown that the coherent solution (23) is self-consistent if $q \ll 1$ (a weak-shear limit) or if $c_s^2 \ll v_A^2$ (a strong-field limit). Therefore, when $v_A^2k_y^2 \neq 0$, any modes that satisfy the instantaneous instability criterion

$$k(t) < k_J \equiv \frac{2\pi G\Sigma_0}{c_s^2}, \quad (24)$$

are subject to a transient or an exponential growth. For fixed $|k|$, ζ is maximized with $k_x = 0$.

Two special cases of equation (23) deserve some comment. When $k_y = 0$, corresponding to axisymmetric modes, the last term in equation (23) vanishes and k becomes a constant. In this case, equation (23) is reduced to the dispersion relation for density waves with a stabilizing role played by magnetic fields (Gammie 1996; Lou & Fan 1998). With $v_A = 0$, one can show that a disk becomes unstable only if $Q < 1$, and the range of unstable wavenumbers is $1 - (1 - Q^2)^{1/2} < k_x/k_{\max} < 1 + (1 - Q^2)^{1/2}$, where $k_{\max} \equiv k_J/2 = \pi G\Sigma_0/c_s^2$. The maximum growth rate is $\zeta_{\max} = c_s k_{\max} (1 - Q^2)^{1/2} = \kappa(Q^{-2} - 1)^{1/2}$ at $k_x = k_{\max}$ (e.g., Shu (1992)). Presence of magnetic fields modifies the Toomre criterion for a hydrodynamic disk in such a way that magnetized disks are unstable to axisymmetric perturbations if $Q_M \equiv \kappa(c_s^2 + v_A^2)^{1/2}/\pi G\Sigma_0 = Q(1 + 1/\beta)^{1/2} < 1$; the maximum unstable wavenumber in a nonrotating disk is given by equation (24) with $c_s^2 \rightarrow (c_s^2 + v_A^2)$, and the fastest growing wavenumber in a rotating disk is half of this. The enhanced axisymmetric stability associated with magnetic fields changes dramatically when nonaxisymmetric modes are considered.

The other interesting limit of equation (23) is rigidly rotating disks with $q = 0$. Without shear, \mathbf{k} is again independent of time, and thus equation (23) is the exact solution to equations (17)-(20). When $q = 0$, the equilibrium may contain nonzero radial magnetic fields, so we may generalize equation (23) by replacing $v_A k_y$ with $\mathbf{v}_A \cdot \mathbf{k}$ in the last term. Magnetic destabilization is apparent and one can easily see that the stability criterion is the 2D Jeans condition: regardless of the magnetic field strength, magnetized disks in rigid-body rotation are subject to nonaxisymmetric

gravitational instabilities if the condition (24) is satisfied. Magnetic tension from bent field lines can reduce the stabilizing effect of the Coriolis force by resisting fluid displacements in the radial direction. When the field is very strong (v_A large; $\beta \ll 1$), motion of gas is mainly parallel to the field lines, so perturbations evolve as if there were no rotation, yielding the same dispersion relation $\zeta^2 = (2\pi G \Sigma_0 |k| - c_s^2 k^2)(\mathbf{v}_A \cdot \mathbf{k})^2 / v_A^2 k^2$ as in a nonrotating, thin disk. With a weak magnetic field ($\beta \gg 1$), the fluid motion is not strictly parallel to field lines and thus growth rates (when $Q > 1$) become small as $\zeta \propto \beta^{-1/2}$. This destabilizing effect of magnetic fields was first studied by Chandrasekhar (1954) for an infinite homogeneous medium and by Lynden-Bell (1966) for a thin galactic disk.³ The detailed physical description is given by Elmegreen (1987a).

3.3. Magneto-Jeans instability *vs.* the magnetically modified swing amplifier

In the general case of nonaxisymmetric perturbations with nonvanishing shear, the secular increase of $k(t)$ would inevitably suppress the development of the instability, implying a transient growth of perturbations: the system is instantaneously unstable only when $|t| < t_c \equiv (K_y^{-2} - 1)^{1/2} / q\Omega$, where $K_y \equiv k_y / k_J$. In order to quantify the virulence of the instability, we define an amplification magnitude as

$$\Gamma \equiv \log \frac{\Sigma_1(t_c)}{\Sigma_1(-t_c)} = 2(\log e) \int_0^{t_c} \zeta(t) dt. \quad (25)$$

Amplification magnitudes for coherent wavelet solutions are easily computed from equations (23) and (25). The resulting Γ for $Q = 1.3$ and $K_y = 0.5$ is displayed in Figure 1 with dotted lines. Also shown as solid lines are the results of direct numerical integrations of the shearing sheet equations (17)-(20). The excellent agreement for small q and/or for small β between the results from the two different approaches demonstrates the validity of the coherent wavelet analysis for the weak-shear or strong-field limit. For $Q \geq 1$ and in the weak-shear limit, the solutions of equations (23) and (25) corresponding to the fastest growing modes that have $K_y = 1/2$ for $\beta \ll 1$ and $K_y \sim 1/2 - 3/4$ for $\beta \gtrsim 0.1$ can be approximated as

$$\Gamma_{\max} = \begin{cases} \frac{2\sqrt{1-q/2}}{qQ}, & \text{for } \beta \ll 1 \text{ and } q \lesssim 1, \\ \frac{1.6}{q\sqrt{\beta}} \frac{1}{Q^2 - f(\beta)}, & \text{for } \beta \gtrsim 0.1 \text{ and } q \lesssim 0.7\beta^{-1/3}Q^{-1}, \end{cases} \quad (26a)$$

$$(26b)$$

where $f(\beta)$ is defined by

$$f(\beta) \equiv 1.17 - \frac{3.97}{(\log \beta + 2.16)^{1.48}}. \quad (27)$$

³Although equation (23) has the same form as equation (1) of Lynden-Bell (1966), equation (23) is more general in the sense that it allows for the solutions with $q \neq 0$ via the value of $\kappa^2 = (4 - 2q)\Omega^2$ and the time dependence of $k_x(t) = k_x + q\Omega k_y t$.

For $10^3 > \beta \geq 1$, $|f(\beta)| < 1$, so that $f(\beta) \simeq 0$ is a good approximation for $Q > 2$. Γ_{\max} from equations (26) and (27) are within $\sim 10\%$ of the results of direct shearing sheet integrations. As both equations (26) and Figure 1 show, $\Gamma \propto q^{-1}$ for $q \ll 1$, which is a manifestation of the longer time interval for the growth of k_x ; in equation (23), the instantaneous growth rate ζ is very weakly dependent on q only through $\kappa^2 = (4 - 2q)\Omega^2$. Equation (26a) gives the maximum amplification amplitude for all β .

One interesting feature in Figure 1 is the β -dependence of Γ obtained from the temporal integration of the shearing sheet equations. When $\beta \ll 1$, Γ is a monotonic function of q , well approximated by the coherent solutions. When $\beta \gg 1$, however, Γ first decreases exponentially with increasing q from zero, becoming vanishingly small at intermediate q , and rapidly rises again to show local maxima at $q \sim 1$. With $q \ll 1$ and $\beta \gg 1$, $\Gamma \propto \beta^{-1/2}$ (see eqs. [26]). In the extreme unmagnetized limit $\beta \rightarrow \infty$, the system is completely stable for $q \ll 1$, while showing moderate growth ($\Gamma \lesssim 1.6$) when $0.2 < q < 2$. Evidently, there are two different types of instabilities. The first kind, operating very efficiently when $\beta \ll 1$, or $q \ll 1$ and $v_A \neq 0$, is similar to the Jeans instability in nonrotating disks. We refer to this as the magneto-Jeans instability (MJJ). In the second type of instability, operating when $\beta \gtrsim 1$ and $q \sim 1$, disturbances grow from the swing amplifier mechanism (GLB; Toomre (1981)) and magnetic fields are not required; in fact, magnetic fields reduce the amplification factor. We refer to this swing-related instability as magnetically-modified swing amplification (MSA).

The contrasting role played by magnetic fields in MJJ and MSA is well illustrated in Figure 2 where we plot Γ with contours on a $Q - \beta$ plane. $K_y = 0.2$ and $q = 1$ are adopted and only the results from temporal integrations of equations (17)-(20) are presented. Notice the discontinuity in Γ that clearly separates the range of β into two parts. Defining β_c as the value of β at the discontinuity, one can see that the MJJ dominates for $\beta < \beta_c$, while a system with $\beta > \beta_c$ is more susceptible to MSA. For a range of the parameters K_y and Q , $\beta_c \sim 0.1 - 1$. For a given Q , Γ attains its minimum at $\beta = \beta_c$. When $\beta > 30$, Γ is almost independent of β , indicating that modification of swing amplification by magnetic fields becomes negligibly small. When $q = 1$, MJJ is less sensitive to Q than MSA is.

As clearly explained by Toomre (1981) and Balbus (1988), hydrodynamic swing amplification arises as a consequence of the conspiracy between three agents: background shear, epicyclic shaking, and self-gravity. Since wave fronts sweep in the same sense as epicycle motions from a leading to a trailing configuration, fluid elements in the wave crests remain longer in the region of excess density, extending their exposure to self-gravity. The net effect is significant growth of the wave amplitude. The fact that swing amplification depends essentially on shear, expressed by the time-dependence of $k_x(t)$, makes MSA different from MJJ, in which shear has only a stabilizing effect. This explains why solutions for MSA cannot be found in the coherent regime that treats $k_x(t)$ as a constant instantaneously⁴. Since rotation curves of spiral galaxies are generally flat (see, e.g., Sofue

⁴Binney & Tremaine (1987) also noted that the spatial WKB approximation fails to capture the swing amplifica-

et al (1999)) with $q \sim 1$ except in small regions very close to their centers, and given the likely condition of near- or sub- equipartition of magnetic energy relative to thermal energy ($\beta \sim 1 - 10$), MSA is expected to be more important than MJJ in the large-scale dynamical evolution of disk galaxies with weak spiral structure. On the other hand, in the central regions of spiral galaxies where rotation curves are almost linear, or in irregular galaxies where shear is relatively weak, MJJ may play a very important role in the formation of molecular clouds.

Previously, these MJJ and MSA modes have been referred to as the swing amplifications of slow and fast MHD density-wave modes, respectively, by Fan & Lou (1997). We adopt our nomenclature because it more transparently refers to the underlying physical mechanisms. Even though slow MHD waves become unstable if the condition (24) is satisfied, it is not precisely a “swing” amplification but more like the 2D Jeans instability with magnetic fields resisting the stabilizing Coriolis force. Moreover, when they grow, MSAs do not maintain as clear wave properties as the fast MHD waves do, as the nonexistence of coherent wavelet solutions for MSAs suggests.

Being isotropic, acoustic waves (or random motions of stars in a stellar disk) affect swing amplification simply by reducing the equivalent gravitational force (JT; Toomre (1981)), and it is sound waves that eventually stop the growth of hydrodynamic swing amplifier. One may ask whether the role of magnetic fields represented by the Alfvén speed v_A is the same as that of c_s in MSA, as is true in the axisymmetric case for MJJ (§3.2). The answer is that magnetic effects instead act as an “anisotropic” reduction factor for self-gravity. The stabilizing effect from magnetic fields is via magnetic pressure. With initial azimuthal fields, however, the magnetic pressure force in the linearized form has only a radial component and requires $k_x \neq 0$. Therefore, stabilization of MSA due to field lines occurs mostly at intermediate pitch angles of the wave fronts, and is vanishingly small when $k_x \sim 0$, while thermal pressure still stabilizes a system even when $k_x = 0$.

In Figure 3, we show the effect of varying K_y on MSA. We take $Q = 1.1, 1.5$ and $q = 1$. Near $K_y \sim 1$, thermal and magnetic pressures cause Γ to decrease rapidly for all β . At the opposite end of the curves, the reduction of Γ with $\beta \rightarrow \infty$ is due to the enhanced relative importance of the epicyclic oscillation that is independent of K_y . For MJJ modes with $\beta \ll 1$, the stabilizing effect from the epicyclic motion appears at small $K_y \sim 0.1\beta$. The discontinuities in Γ on the $\beta = 1$ curves again emphasize the existence of two different instabilities: MSA operates with small K_y , while strong tension forces with large K_y favor MJJ.

A recurring issue in studying dynamics of massive disks is the question of how large a scale must be considered, due to the nonlocal nature of gravity. Balbus & Papaloizou (1999), for example, suggest that angular momentum transport by gravitational torques should be studied in the framework of a global rather than local model, although they point out that this is less of an issue for disks with Q near unity, because wave propagation is less important. Note that for $\beta \geq 1$, we find (see e.g., Fig. 3) maximum values of Γ are achieved at $K_y \sim 0.15 - 0.4$, corresponding to a

tion.

few kpc from equation (10). This implies that the local model we will adopt for our simulation study is somewhat marginal as a direct representation of a small piece of a galactic disk. In spite of this caveat, we believe the model still captures the important features of instabilities growing in self-gravitating, thin disks, at least as long as $\beta \geq 1$. We discuss checks of this obtained by varying the simulation box size, in §6.

To summarize this section, we found that shearing, self-gravitating disks with embedded magnetic fields are unstable to two kinds of nonaxisymmetric instabilities: (1) the magneto-Jeans instability, which works efficiently in a strongly magnetized medium or in a medium with weak shear, and (2) magnetically-modified swing amplification, which works in a moderately or weakly magnetized medium with relatively strong shear. Increased magnetic fields tend to destabilize the former, while stabilizing the latter. We provided coherent wavelet solutions applicable to MJJ.

4. Numerical method and code tests

To follow the nonlinear evolution of gravitational instabilities in shearing, magnetized disks, we integrate equations (1)-(6) using a modified version of the ZEUS code for numerical MHD (Stone & Norman 1992a,b). ZEUS uses a time-explicit, operator-split, finite-difference method to solve the MHD equations on a staggered mesh. The MHD algorithm employs the constrained-transport formalism to maintain the condition $\nabla \cdot \mathbf{B} = 0$ within machine precision, and the method of characteristics for accurate propagation of Alfvén waves (Evans & Hawley 1988; Hawley & Stone 1995). For the advection of the hydrodynamic variables, we decompose the azimuthal direction ($\hat{\mathbf{y}}$) velocity into the mean shearing part and the remaining perturbed part, and transport only the perturbed terms with ZEUS’s advection algorithm, while treating the contribution arising from the mean shearing part as source terms⁵. Through an advection test of a square pulse moving across the radial boundaries, we confirmed that the velocity decomposition method gives less diffusive results than does transport involving the whole velocity, especially when the mean shearing velocity is comparable to or larger than the transverse velocity component. Another numerical method for treating a strongly supersonic shear flow in a non-self-gravitating, unmagnetized medium is described by Masset (2000); a similar technique was adopted by Gammie (2001).

We apply shearing box boundary conditions in which the azimuthal boundaries are perfectly periodic and the radial boundaries are shearing-periodic. In the absence of initial radial magnetic

⁵If we decompose the velocity as $\mathbf{v} = \mathbf{v}_0 + \delta\mathbf{v}$, the advection term of the $\hat{\mathbf{y}}$ -momentum due to the perturbed velocity in conservative form appears as $\nabla \cdot (\Sigma v_0 \delta\mathbf{v}) = -q\Omega\Sigma\delta v_x + v_0\nabla \cdot (\Sigma\delta\mathbf{v})$, the first term of which can be evaluated in the source step. There are various ways to compute $\Sigma\delta v_x$ in a finite difference scheme, but we found that

$$\Sigma\delta v_x \Big|_{i,j} = \frac{1}{4} \left[\Sigma_{i,j}(\delta v_{x,i+1,j} + \delta v_{x,i,j}) + \Sigma_{i,j-1}(\delta v_{x,i+1,j-1} + \delta v_{x,i,j-1}) \right],$$

gives the most accurate results. Here, the indices i and j denote respectively the x - and y -coordinates of a spatial staggered grid point defined in the ZEUS code.

flux, the shearing box boundary conditions conserve the total magnetic flux through each surface of the sheared box; the long-time average through the $\hat{\mathbf{y}}$ -surfaces of the computational box is then also uniform. The volume-integrated total energy in a shearing box is not a conserved quantity; its rate of change is determined by the angular momentum flux associated with Reynolds, Maxwell, and gravitational stresses across the radial surfaces (Hawley, Gammie, & Balbus 1995; Balbus & Papaloizou 1999; Gammie 2001). We implemented the remap algorithm discussed by Hawley, Gammie, & Balbus (1995) in which the physical values at the ghost zones adjacent to one radial boundary are remapped in the Lagrangian sense from the values at the active zones on the other radial boundary. Because of the opposite background velocities, however, the flow characteristics at each radial boundary are quite different from each other. After the remap procedure, therefore, discontinuities in the flow characteristics are unavoidable across the radial boundaries, tending to generate vorticity when fluid moves across the radial boundaries and adding noise to propagating Alfvén waves. We address this problem by keeping the ghost zones adjoining the radial boundaries active in the transport step along the $\hat{\mathbf{y}}$ -direction.

The solution of the Poisson equation is obtained by the Fourier transform method modified by the shearing box boundary condition, as discussed by Gammie (2001). Since the density distribution at an arbitrary time is not periodic in the $\hat{\mathbf{x}}$ -direction, we transform to sheared coordinates, $x' = x, y' = y + q\Omega x(t - t_p)$, after finding the nearest time t_p (either positive or negative) that gives an exactly periodic distribution in the transformed coordinate. We solve the Poisson equation using the standard discrete fast Fourier transform technique in the primed coordinates and then transform the calculated potential back into the simulation domain. To make the gravitational force isotropic on small scales, we discard the modes with $|k| > 2^{-1/2}(N/2)(2\pi/L)$, where $N \times N$ is the numerical resolution.

For most of our simulations (except where noted), initial perturbations are realized by a Gaussian random density field with a power spectrum $\langle |\Sigma_k|^2 \rangle \propto k^{-8/3}$ for $2\pi/L \leq k \leq (N/2)(2\pi/L)$. If the perturbations arise from motions obeying a sonic dispersion relation ($\omega \sim c_s k$), this corresponds to the 2D Kolmogorov velocity spectrum that gives a conservative cascade of energy transfer. This choice of power spectrum is to some extent arbitrary; one may argue, for example, whether a Kolmogorov or Burgers power spectrum is more appropriate. Through the numerical simulations, however, we have confirmed that the particular choice of spectral index does not make a large difference, as long as the power spectrum is decreasing at large k . We measure the standard deviation ϵ_0 of the initial density fluctuations $\Sigma/\Sigma_0 - 1$ in real space, and use this value to parameterize the initial perturbation amplitudes; we allow ϵ_0 to vary from 10^{-3} to 10^{-2} .

4.1. Code tests

We have verified our numerical algorithm with a wide variety of test problems: MHD shock tubes and propagation of polarized Alfvén waves in nonshearing medium, advection of a square box with enhanced density in a background shear flow, axisymmetric traveling and standing MHD

waves modified by self-gravity and shear, and axisymmetric gravitational instabilities with shear. By comparing the results with corresponding analytic predictions, we have confirmed the code’s performance.

Of particular importance for the current work is the test calculation of linear, nonaxisymmetric gravitational instabilities, because this test can directly verify the correctness of our implementation of the boundary condition and the Poisson solver. In order to compare with the results of linear analysis, we initially apply very small amplitude sinusoidal perturbations, $\Sigma_1 = \epsilon_0 \cos(k_x x + k_y y)$, $v_{y,1} = \epsilon_0 \sin(k_x x + k_y y)$, and $B_{x,1} = \epsilon_0 k_y / 2\pi \cos(k_x x + k_y y)$; the initial conditions for the other variables were determined by imposing the requirements of adiabatic, zero-vorticity, $\nabla \cdot \mathbf{B}_1 = 0$ perturbations. The other chosen parameters are $Q = 2$, $n_J = 2.5$, $q = 1$, $\gamma = 1.5$, $\beta = 1$, $\epsilon_0 = 10^{-4}$, $k_x / 2\pi = -6$, and $k_y / 2\pi = 1$. In Figure 4 we display with solid line the Eulerian time evolutions of the variables at a location $(x, y) = (-0.07, 0.28)$ from a 128^2 -zone simulation, which are in excellent agreement with the results from linear analysis plotted by open circles. During the swing amplification ($t \sim 2 - 9$) phase, the system experiences an increase of density by a factor of 25. As time increases the MSA phase ends and density oscillates in accordance with the passage of waves of high k . For all the variables, a small discrepancy between linear and nonlinear solutions is observed at $t \sim 10 - 12$. This is not an error related to the numerical scheme. Rather, this is due to modulation of the wave mode of our interest with waves that are generated from nonlinear effects and subsequently grow with swing amplification.

5. Nonlinear evolution of magneto-Jeans instability

Following up the linear analysis of MJI in §3, we have performed numerical simulations of the development of these instabilities in a medium with weak shear, adopting $Q = 1.5$, $n_J = 5$, $q = 0$ or 0.1 , and $\beta = 1$, while varying γ from 1 to 2. We initially perturbed a uniform density medium by applying white noise perturbations⁶ of amplitude $10^{-3}\Sigma_0$, and then evolved the system up to $t/t_{\text{orb}} = 4$. The resulting time histories of the maximum density for $q = 0.1$ and varying γ are plotted in Figure 5. For comparison, we also plot with dotted line the result from the simulation with $q = 0$ and $\gamma = 1$, for which the kinematic stabilization of MJIs is absent. Exemplary snapshots of density structures, perturbed velocity, and magnetic field lines at $t/t_{\text{orb}} = 2, 4$ of the $\gamma = 2$ simulation are displayed in Figure 6.

Initially, all the modes that satisfy the instantaneous instability criterion (24) begin to grow,

⁶Since the fastest growing mode has $k_y = 3.3(2\pi/L)$ for the chosen parameters, power-law perturbations that have most of the power at $k_y \simeq 0$ would exhibit complicated behavior in the evolution of maximum surface density at early times, as the initial growth of low- k modes is succeeded by faster-growing but initially lower-amplitude higher- k modes. In order to study the modal growth of perturbations as cleanly as possible, we have instead imposed white noise perturbations for these MJI simulations. Because MJIs with $q \ll 1$ yield almost exponential growth, the final state, always dominated by the most unstable modes, is quite independent of the type of applied perturbation.

and subsequently the system becomes dominated by the most unstable mode. With the chosen parameters, the coherent wavelet solutions predict that the mode with $K_y = 0.66$ corresponding to $k_y = 3.3(2\pi/L)$ has the largest instantaneous growth rate at $k_x = 0$. When the system is rigidly rotating with $q = 0$, this mode is expected to continue to grow exponentially without limit. When $q = 0.1$, on the other hand, this mode is allowed to grow only until $t/t_{\text{orb}} = 3.6$ when the radial wavenumber increases up to $k_x(t) \simeq 3.8(2\pi/L)$, forming corrugated stripes with a pitch angle $\phi \equiv \tan^{-1}(k_y/k_x) = 41^\circ$. Beyond this time, thermal pressure dominates self-gravity and no further growth is expected. The estimated total amplification for the $q = 0.1$ case is about 8 orders of magnitude.

The linear prediction for the most unstable mode is indeed shown in the simulations. Figure 5 shows that for $q = 0$, the density increases exponentially with time until nonlinear effects control the dynamics. With the isothermal equation of state, the density rises more rapidly as the overdense regions start to collapse nonlinearly. The growth rates of the maximum density for $q = 0.1$ are not much different from the rigidly rotating case, because k_x remains small throughout the linear phase. In fact, the maximum pitch angle attained before the nonlinear effects become significant is $\phi \sim 53^\circ$ corresponding to $k_x = 2.5(2\pi/L)$ (see, for example, Figure 6), indicating that kinematic stabilization from shear never occurs. The late nonlinear phase (but not the linear phase) of MJI is very sensitive to the choice of γ . When γ is close to 1, overdense stripes collapse rapidly as they form mainly along the azimuthal direction. As γ increases, the collapse is progressively delayed so that the stripes have more time to be sheared out. If the perturbed velocity field has grown almost comparable to or even greater than the background shear velocity, the azimuthal shear rate is also locally modified substantially from the initial value. Gravitational attraction between neighboring stripes also changes the shear rate significantly, causing them eventually to collide with each other. The result is the formation of a few big condensations. When $\gamma < 1.6$, the condensed lumps keep collapsing towards their centers, making it difficult to follow the subsequent evolution. We stop the simulation when the central density of the biggest lump becomes so high that we are not able to spatially resolve the central region. In general, in order to prevent spurious results arising from limited numerical resolution, the local grid scale must be smaller than the smallest local gravitationally unstable wavelength (Truelove et al 1997, 1998); since the instantaneous value of k_J (eq. [24]) increases with increasing Σ , any unstable low- γ simulation on a fixed grid eventually becomes unresolved.

When $\gamma \gtrsim 1.6$, on the other hand, a stiff equation of state provides the strong thermal pressure gradient to halt gravitational collapse, and form gravitationally bound clumps. The right frame of Figure 6, for example, shows a disk consisting of 4 clumps and ridges connecting them. The two biggest clumps to the left have each 32% and 17% of the total mass. Additional support from magnetic pressure makes them elongated across the field lines. The field strength is correlated with the surface density roughly as $B \sim \Sigma^{0.5}$. Clumps grow slowly as they accrete material and then experience collisional agglomeration to form ultimately one large object, after $t/t_{\text{orb}} = 5.4$.

6. Nonlinear evolution of magnetically modified swing amplification

In the previous section, we showed that when shear is very low, rotating, magnetized, self-gravitating systems are unstable to nonaxisymmetric disturbances, eventually collapsing or forming gravitationally bound condensations within ~ 2 orbital times. This result is interesting in the sense that inclusion of magnetic fields modifies the dynamics significantly, permitting instability even when $Q > 1$, possibly accounting for the active star formation towards centers of galaxies (cf. Kenney et al (1993); Kennicutt (1998); Martin & Kennicutt (2001)). However, the majority of material in spiral galaxies in fact orbits subject to a flat rotation curve (at least away from strong spiral arms). With such strong shear, MJI is disabled, but MSA becomes active. To explore nonlinear evolution of such high-shear regions under MSA, we have carried out extensive simulations by fixing $q = 1$ and varying other input conditions.

6.1. Hydrodynamic case

Table 1 lists the various parameters for simulations following the nonlinear evolution of swing amplification in purely hydrodynamic disks. The first column labels each run with the prefix H and a model number. The second and third columns give the two basic parameters of our simulations: Toomre’s stability parameter Q and the Jeans number n_J of the simulation box (see eqs. [7] and [8]). The 2D adiabatic index for the equation of state is given in the fourth column, while the fifth column gives the amplitude of initial perturbations indicated in terms of the standard deviation ϵ_0 of density fluctuations. The numerical resolution is shown in the sixth column. The next two columns list the termination time τ_{1st} of the MSA and the amplification magnitude Γ_{1st} that measures the growth in the standard deviation of the density distribution at $t = \tau_{1st}$ determined from the simulation results. The time τ_{1st} is defined as the time corresponding to the first local maximum in the evolutionary history of the RMS density fluctuation, $\epsilon \equiv \langle (\Sigma/\Sigma_0 - 1)^2 \rangle^{1/2}$. Times are given in units of t_{orb} (see eq. [13]). The ninth column gives the time when the nonlinear secondary instability (see below) begins. The final simulation outcome (i.e. within $4t_{orb}$) is given in the final column where “Unstable” means a runaway collapse or the formation of condensation, while “Stable” means low-amplitude wave motion at the end of the simulation. Cases that do not produce any condensations but fluctuate with large amplitude are identified as “Marginal”.

Evolutionary histories of a standard set of the hydrodynamic simulations are shown in Figure 7, where we plot the variations of maximum surface densities over time⁷. The evolution of the RMS density fluctuation amplitude ϵ shows similar behavior. We fix $q = 1$, $n_J = 5$, $\gamma = 1.5$ and vary ϵ_0 and Q . It is clear that for all cases the initial phase of evolution is governed by swing amplification, exhibiting rapid growth of the surface density. While these initial swing amplifications in $Q \gtrsim 0.9$ models become saturated at $t/t_{orb} \sim 0.6 - 0.9$ from shear kinematics, nonlinear collapse of shearing

⁷Our realization of initial density perturbations has the maximum density $\Sigma_{max}/\Sigma_0 = 1 + 3.5\epsilon_0$ at $t = 0$.

wavelets immediately and continuously follows the initial swing amplifications when $Q \lesssim 0.8$ (models H06 and H07). Fourier analyses of the density distributions at each time when the shearing box becomes exactly periodic reveal that the dominant mode during the swing amplification phase of these models has $k_y = 1(2\pi/L)$. From the linear theory, Figure 3 shows the total amplification of modes for $Q = 1.1$ and 1.5 and $q = 1$ as a function of K_y , where $k_y = K_y n_J (2\pi/L)$. The maximum amplification predicted is for $K_y = 0.2 - 0.3$ corresponding to $k_y = (1 - 1.5) \times (2\pi/L)$ for $n_J = 5$, in good agreement with the simulations⁸. As noted above, the growth times and the amplification magnitudes from the numerical simulations are listed in the seventh and eighth columns of Table 1. For these columns we also list in parentheses the termination times t_c and corresponding growth magnitudes for swing amplification of the $K_y = 0.2$ modes in the linear theory, determined by integration of equations (17)-(20) from $t = 0$ to $t = t_c$ (i.e. approximately half of the full swing interval). For $1 \leq Q \leq 1.4$, if a mode were allowed to grow from $t = -t_c$, its amplification factor would be $\sim 3 - 10$ times greater than that of a half swing. The contribution from the initial modes with $k_x < 0$ that undergo a full swing amplification in the simulation is very small, because the steep power spectrum sets the amplitudes of these $k_x \neq 0, k_y \neq 0$ modes as small compared to the amplitudes of the corresponding $k_x = 0, k_y = 0$ modes.

While the fluctuation amplitudes vary slowly and continuously with the parameter Q during the initial swing phase, the subsequent nonlinear evolution is critically dependent on Q , exhibiting “threshold” behavior. For the time being, we concentrate our discussion on the $\epsilon_0 = 10^{-2}$ cases. When $Q \lesssim 0.8$, as in model H06 and H07, the density enhancement from swing is so large that shearing wavelets produce overdense filaments, which become gravitationally unstable along their length, even before swing amplification ends. The filaments collapse and fragment further into pieces at $t/t_{\text{orb}} \sim 0.5$. Model H06, for instance, forms six fragments with each mass in the range of $\sim 2-7\%$ of the total mass, which can be compared with a characteristic Jeans mass of 4% for $n_J = 5$. The fragments subsequently collect background material and collide with each other to form larger clumps each of mass $\sim 8-28\%$ at $t/t_{\text{orb}} \sim 0.8$. When Q is intermediate, as in models H08 ($Q = 0.9$) and H09 ($Q = 1.0$), on the other hand, the growth of surface density from swing amplification is not enough to initiate the collapse of the shearing wavelets, and thus parallel fragmentation does not occur. Since the swing-amplified perturbations modify the initial background velocity field significantly, the filamentary structures can also move in the radial direction, and may collide with other filaments that are moving in the opposite direction. The mutual gravitational forces between the moving filaments expedite physical collisions. With their larger surface density, the filaments in model H08 collide more violently than those in model H09, quickly leading to the formation of four bound clumps at $t/t_{\text{orb}} \sim 1.0$. Model H09 experiences five successive collisions of wavelets to form one big clump at $t/t_{\text{orb}} \sim 2.2$, as shown in Figure 8.

When $Q \gtrsim 1.1$, swing amplification is so mild that it produces neither immediate parallel fragmentation of filaments, nor physical collision of filaments followed by fragmentation. In this case,

⁸Recall that $k_y(2\pi/L)^{-1}$ can only take on integer values in the simulations.

the transient swing amplification saturates into an “intermediate” state with many independent perturbations with small radial wavelengths. When $Q \gtrsim 1.3$, the amplitude of perturbations at the end of the swing phase is quite low, and thus the perturbed surface density remains always in the linear regime throughout the evolution, showing no further growth beyond the intermediate-saturation state. If $1.3 > Q \gtrsim 1.1$, however, swing amplification casts the system into a pivotal state where shearing wavelets nonlinearly interact with each other (but not involving physical collisions). While the linear phase is characterized by the steady, kinematic increase of the radial wavenumber (verified directly by examination of Fourier amplitudes), nonlinear interactions among different modes in this pivotal state can change the radial wavenumber dynamically, causing new small- $|k_x|$ modes to be produced. These newly excited, small- $|k_x|$ modes are subject to swing amplification, and grow further. If the nonlinear feedback is strong enough, the result of this “rejuvenated swing” is the formation of gravitationally bound condensations (see below). With only moderate feedback, however, the models H10 and H11 (with $Q = 1.1$ and 1.2) have only fluctuating density fields with order-unity amplitudes, with strong shear preventing clumps from forming up to the limit of our integration.

Obviously, the $\epsilon_0 = 10^{-3}$ models are more stable than their $\epsilon_0 = 10^{-2}$ counterparts, mostly because the shear instability is only transient. When $\epsilon_0 = 10^{-3}$, $Q \gtrsim 1.1$ models remain stable, never entering a nonlinear stage. Model H01 ($Q = 0.9$) becomes unstable via the direct collisions of filaments, while nonlinear feedback allowing rejuvenated swing amplification makes model H02 ($Q = 1.0$) eventually unstable. In spite of the different paths to the formation of gravitationally bound objects, Figure 7 suggests that reduction of ϵ_0 by a factor of 10 does not significantly alter the critical Q -value that discriminates between collapsing and non-collapsing simulation outcomes; the nonlinear stability of self-gravitating, shearing disks is relatively insensitive to the initial perturbation amplitude. The value Q_c , above which gravitationally bound objects do not form, is in the range $\sim 1.1 - 1.3$ for these unmagnetized models.

Elmegreen (1991) studied cloud formation via the combination of Parker, thermal, and gravitational instabilities, and argued that gravitational instability of higher density filaments first grown from the swing mechanism could form discrete clouds. He termed this parallel fragmentation process the “secondary” gravitational instability. Our simulations indicate that there are two additional processes that could potentially lead to gravitationally bound condensations: physical collisions of filaments, and rejuvenated swing amplification following nonlinear feedback creating small- $|k_x|$ modes. In what follows, we shall use *secondary instability* to include all three routes mentioned above. The ninth column τ_{2nd} in Table 1 lists the time when filaments start to fragment or collide, or secondary swing amplifications occur. We will continue the discussion of secondary instabilities in §6.3.

Figure 8 shows comparative density snapshots at three different epochs, for the $\epsilon_0 = 10^{-2}$ models H09 with $Q = 1.0$ (left column) and H13 with $Q = 1.4$ (right column). Density structure is shown in logarithmic scale. It is found that at the end of initial swing amplification the potential vorticity $\xi \equiv |\nabla \times \mathbf{v} + 2\mathbf{\Omega}|/\Sigma$ is maintained with its initial equilibrium value $\xi_0 = (2 - q)\Omega/\Sigma_0$

within $\sim 4\%$ except the regions where shocks form, confirming that in the absence of viscosity and magnetic fields, potential vorticity is conserved (e.g., Hunter (1964); Gammie (1996, 2001)). (Here, Ω is the angular velocity of the grid center at $x = y = 0$.) Small deviations of ξ from ξ_0 are due to our non-isentropic initial density perturbations. A consequence of this potential vorticity conservation in steady flow is the modification of the local epicycle frequency as $\kappa = \kappa_0(\Sigma/\Sigma_0)^{1/2}$ (Balbus & Cowie 1985; Dworkadas & Balbus 1996), allowing for the correlation between local shear rate $q_1 \equiv -\Omega^{-1}dv_y/dx$ and surface density as $q_1 = 2 - (2 - q)\Sigma/\Sigma_0$, when the motion is predominantly azimuthal. Nonsteady and/or radial flows would alter this correlation, and both models H09 and H13 (with $q = 1$) exhibit $q_1 \sim 1.6 - 0.6\Sigma/\Sigma_0$. That is, the local azimuthal shear rate decreases with increasing surface density similarly to but not exactly following the prediction for steady, purely-azimuthal flow. Since the streamlines emanating from the shock fronts begin to be mixed up as shearing wavelets start to nonlinearly interact, the potential vorticity is not conserved over the entire domain at the end of the simulations. It is apparent from Figure 8 that when $Q = 1.4$, perturbations do not grow enough to become nonlinearly unstable, but instead become essentially sheared sonic oscillations. At $t/t_{\text{orb}} = 3$, the oscillation amplitude of density is $\sim 12\%$ of the background density and the radial wavenumber has been increased by shear up to $k_x \simeq 19(2\pi/L)$. When $Q = 1.0$, on the other hand, successive collisions of nonlinear sheared patches induced by gravity eventually form a condensation whose mass is 28% of the total mass in the simulation domain.

We explore the effect of γ on the simulation outcome first by comparing model H09 ($\gamma = 1.5$) with models H14 and H18 (with $\gamma = 1$ and 2, respectively), as displayed in Figure 9a for the $Q = 1$ models. Although the initial evolution of surface density is independent of γ , higher γ can reduce the effect of self-gravity once density grows sufficiently, lowering the saturation level of the initial swing amplification. For example, the saturated density at the end of the swing phase in model H18 with $\gamma = 2$ is 15% smaller than that of model H09 with $\gamma = 1.5$. Subsequent nonlinear interaction among wavelets is less active than in the $\gamma = 1.5$ case as well. Nonlinear feedback is strong enough to increase the density in the $\gamma = 2$ model up to $7 \Sigma_0$ at $t/t_{\text{orb}} = 1.5$, but a pressure bounce resulting from the (unphysically) stiff equation of state combines with the background shear velocity field to prevent formation of a condensation. On the other hand, in model H14 with $\gamma = 1$ – just as for the $\gamma = 1.5$ model H09 – shearing wavelets start to collapse before the swing amplification ends, and thermal pressure gradients are insufficient to halt gravitational runaway. As the collapse proceeds, fragmentation occurs (our resolution here $[256^2]$ is not adequate to follow late-time evolution of fragments). Models H11 to H13 with $\gamma = 1.5$ (shown in Fig. 7b) similarly may be compared with their $\gamma = 1$ counterparts, H15 to H17 (shown in Fig. 9a). In Model H15 with $Q = 1.2$ and $\gamma = 1$, the saturation level of surface density is higher than model H11 with $\gamma = 1.5$, but not enough to be unstable immediately. Instability is deferred until $t/t_{\text{orb}} \sim 2$, when much more vigorous nonlinear feedback drives the system into gravitational collapse. As Q increases further, no secondary instability occurs; even with $\gamma = 1$, a local disk with $Q \geq 1.3$ is stable to forming self-gravitating condensations. Overall, we conclude that the Q threshold for nonlinear gravitational instability is relatively insensitive to the value of γ , decreasing by at most ≈ 0.2 as γ

increases from 1 to 1.5.

To assess the extent to which our local approximation may affect the dynamics, we have performed a number of simulations in which we vary the size of the local box. In §3, we argued that the local model should be acceptable for the study of linear MSA because the maximum amplification is achieved at intermediate wavenumbers. We test whether the nonlinear outcome of MSA is indeed insensitive to the box size by repeating models H09 and H11 (with $n_J = 5$) as models H20 and H21 in domains four times as large in area (with $n_J = 10$). These $n_J = 10$ models can harbor modes with wavelengths twice as large as the maximum permitted in the $n_J = 5$ models under the periodic box boundary conditions. If the inclusion of $\lambda = 2L$ modes were to produce significant changes in simulation outcomes, our approach of investigating gravitational stability of galactic disks using a local model would come into question. Reassuringly, results presented in Figure 9b show that the evolution of maximum surface density in $n_J = 10$ models is in fact quite similar to that in $n_J = 5$ models⁹, although the presence of $\lambda = 2L$ modes in model H20 induce more violent late time evolution in collapsing objects, starting at $t/t_{\text{orb}} \sim 1.5$. As a result of its higher total mass, model H20 forms more strongly bound clumps than model H09, but in terms of instability criteria, $n_J = 10$ models yield the same result as $n_J = 5$ models. These (and similar) experiments confirm that the local model is an acceptable tool to study stability of disks, provided the box size is large enough to contain the dominant growing modes.

Finally, we have confirmed that our standard resolution of 256^2 is adequate for the current purpose by comparing models at varying resolution. Figure 9c shows, for example, the comparison of models H11 with identical models at twice and half the numerical resolution (H22, H23). Since k_x is expected to increase linearly with time, we need to make sure that nonlinear secondary instability is not an artificial result arising from insufficient late-time resolution of high- k_x modes. The results shown in Figure 9c indicate that the secondary instability is authentic, occurring at the same time ($t/t_{\text{orb}} \sim 2.1$) regardless of the resolution. In fact, during the time interval $0.7 < t/t_{\text{orb}} < 2.1$, most of power remains below $k_x = 10(2\pi/L)$ for these models; we find similarly that for other models in which secondary instability develops, $k_x \lesssim 10(2\pi/L)$ modes during the saturated intermediate state. This suggests that nonlinear (or perhaps quasilinear) interactions of wavelets are continuously feeding power back into the low- $|k_x|$ regime, preventing the secular kinematic increase of radial wavenumbers that would otherwise occur absent such interactions (see Fig. 4).

⁹A simulation box with n_J can accommodate modes that satisfy $K_y = j/n_J$, where j is any positive integer between 1 and half the number of resolution elements in the $\hat{\mathbf{y}}$ -direction. From Figure 3a, one can expect that $n_J = 10$ models have an additional, small contribution from $K_y = 0.1$ modes that are absent in $n_J = 5$ models in the initial swing amplification.

6.2. Magnetohydrodynamic case

To study the effect of the magnetic field on the nonlinear evolution of local shearing disks, we have performed a number of shearing box simulations in which we include a purely toroidal initial field with strength given by $\beta = 10$ or 1 (see eq. [11] for normalization). The parameters and evolutionary characteristics of the simulations, each designated by the prefix M and a model number, are listed in Table 2. For all of these MHD simulations, a 256^2 grid was used. When shear is relatively strong ($q \sim 1$), as described in §3, the presence of a magnetic field tends to play a stabilizing role in the linear phase of amplification. In the previous section, we showed that nonlinear secondary instabilities can destabilize a hydrodynamic system that would otherwise be ultimately stable. The importance of secondary instabilities in a magnetized system may differ from the hydrodynamic case, and thus the primary question we address in this section is how the eventual fate of a system is modified by the inclusion of a magnetic field.

We plot the evolution of maximum surface density in Figure 10 for $\beta = 10$ cases (models M01-M14) and in Figure 11 for $\beta = 1$ cases (models M15-M26), respectively. As expected from the linear theory, the magnetic pressure from embedded mean toroidal fields reduces the effect of self-gravity along the radial direction, causing MSA to cease earlier, and thus reducing corresponding initial amplification factors by, e.g., 37% for $\beta = 10$ and 90% for $\beta = 1$, compared to the unmagnetized case with $Q = 1.0$. Magnetic tension resists the Coriolis force, reducing the amplitude of the perturbed radial velocities, but this effect is not significant if shear is strong *and* the initial field strength is relatively weak ($\beta \geq 1$). Unlike in the axisymmetric case, the simple replacement of Q with $Q_M \equiv Q(1 + 1/\beta)^{1/2}$ does not accurately represent the effects of magnetic fields in MSA compared to swing amplification.

As in the hydrodynamic cases, the models with $\epsilon_0 = 10^{-2}$ and $Q \lesssim 0.8$ (M05, M06 with $\beta = 10$; M19, M20 with $\beta = 1$) all experience parallel fragmentation of filaments before MSA terminates, while gravitationally-induced collisions of filaments dominate the nonlinear stage in slightly higher- Q models such as M07 and M08 (respectively with $Q = 0.9, 1.0$ and $\beta = 10$), and M21 (with $Q = 0.9$ and $\beta = 1$). The comparison of the evolutionary histories of $Q = 1$ models M08 (in Fig. 10) and H09 (in Fig. 7) shows that embedded magnetic fields make evolution in the aftermath of collisions more violent, by removing the constraint of the potential vorticity conservation. As a result, model M08 rapidly forms four bound clumps within $t/t_{\text{orb}} \sim 1.6$, whereas model H09 forms a clump at $t/t_{\text{orb}} \sim 2.2$, as explained before. Because MSA yields a lower amplification of perturbations for smaller- β models, however, model M22 (with $Q = 1.0$ and $\beta = 1$) does not show physical collisions of shearing wavelets to form condensations. Instead, model M22 becomes nonlinearly unstable through a secondary swing amplification.

In intermediate- Q models in which parallel fragmentation and collisions of filaments do not occur, shearing wavelets interact nonlinearly after the initial MSA phase ends, as in the intermediate- Q hydrodynamic models. With magnetic fields included, however, these nonlinear interactions are much stronger, more easily leading to formation of condensations via “rejuvenated” MSA. The

best examples for nonlinear magnetic destabilization are found in models M10 (with $Q = 1.2$ and $\beta = 10$) and M23 (with $Q = 1.1$ and $\beta = 1$). The corresponding unmagnetized models (H11 and H10, respectively) are only marginally stable. Snapshots of density and field configurations of these unstable magnetized M10 and M23 models, at three selected times, are respectively shown in Figures 12 and 13, where we also display for comparison stable magnetized models M13 and M25 with slightly larger Q . Although the saturation level of surface density fluctuations from the initial MSA is lower than from unmagnetized swing amplification with same Q , magnetic field lines that connect shearing wavelets enhance nonlinear interaction and limit the growth of k_x below $8(2\pi/L)$ for models M10 and M23. Small- $|k_x|$ modes are replenished by nonlinear interactions, and then grow further through secondary MSAs to dominate the evolution. The left-middle snapshots in Figures 12 and 13 clearly show the density structures associated with secondary swing amplification; notice that the pitch angles in these snapshots are larger (indicating smaller k_x) than the pitch angles in the upper (earlier) frames. The condensations in model M10 formed as a consequence of secondary instability have 13%, 8%, and 5% of the total mass from left to right, while model M23 has two condensations with mass each 24% and 10% from left to right. Notice, from model M10 in Figure 12, the characteristic signature of prograde rotation in the collapsed condensations evident from the wrapping of embedded field lines.

In §6.1, we showed from hydrodynamic simulations that unmagnetized, isentropic flows indeed conserve the potential vorticity ξ ; i.e., they maintain a strict linear relationship between vorticity and surface density along a given streamline. The presence of magnetic fields must, however, destroy potential vorticity conservation (e.g., Gammie (1996)). With relatively weak magnetic fields ($\beta = 10$), model M10 at the end of swing amplifications still exhibits a weak correlation between vorticity and surface density, giving $\xi = (1 \pm 0.2)\xi_0$. In model M23 with $\beta = 1$, however, vorticity does not correlate with surface density at all throughout the evolution; the local shear rate at any point is totally independent of the surface density. Unlike the situation within spiral arms for pure hydrodynamics, therefore, the local shear rate within spiral arms for an MHD flow need not be a decreasing function of the surface density, depending on field alignment.

Experiments with different γ , with histories presented in Figure 14a, demonstrate that γ only affects the strongly nonlinear phase, and does not generically alter the ultimate simulation outcome. In particular, for $\gamma = 1$ and 1.5, there is no measured difference (i.e. < 0.1) in the gravitational runaway threshold levels Q_c . Figure 14b compares evolutionary histories with varying simulation box sizes. In general the initial growth of surface density is slightly larger in $n_J = 10$ models than in $n_J = 5$ cases, and differences of the growth factors between the models with $\beta = 1$ are slightly larger than in hydrodynamic cases. This is because, as indicated by Figure 3, the relative importance of $K_y = 0.1$ modes (that fit in $n_J = 10$ but not $n_J = 5$ boxes) to $K_y = 0.2$ modes (that fit in both boxes) is larger when $\beta = 1$ than when $\beta = \infty$. Nevertheless, the simulation box size makes negligible difference to the computed nonlinear stability criterion, again supporting the appropriateness of a local model for the study of disk stability. Finally, we have performed a set of simulations (models M35 to M38) taking the 2D Burgers power spectrum $\langle |\Sigma_k|^2 \rangle \propto k^{-3}$ as an initial

density perturbation. The results are shown in Figure 14c together with models M22 to M25, which start with a 2D Kolmogorov spectrum. Although the 2D Burgers spectrum leads to $\sim 4 - 13\%$ higher saturation levels, the overall evolutionary behaviors, especially final outcomes of models M35 to M38, are essentially indistinguishable from those of model M22 to M25. This confirms that the gravitational instability criteria obtained from numerical simulations are independent of the adopted initial perturbation spectra, as long as the power decreases as the wavenumber increases.

Even with embedded magnetized fields, models having relatively large Q are unable to reach the regime where nonlinear feedback is strong enough to induce a secondary instability. With $\epsilon_0 = 10^{-2}$, we find critical Q values $Q_c = 1.4$ for $\beta = 10$ and $Q_c = 1.2$ for $\beta = 1$. These thresholds are subject to slight change if initial perturbation amplitudes vary; Figures 10 and 11 show that the Q_c values increase by $\lesssim 0.3$ as ϵ_0 increases by a factor ten. This behavior attests to the fact that intermediate saturation is caused not by nonlinear effects but by the transient nature of MSA. Compared to the hydrodynamic critical value $Q_c = 1.3$, the higher critical value $Q_c = 1.4$ in the $\beta = 10$ sub-thermally magnetized system indicates that stronger nonlinear feedback renders it more unstable, while the lower critical value $Q_c = 1.2$ in $\beta = 1$ models, indicative of greater stability, arises from a lower growth in the initial MSA phase.

6.3. Routes to structure formation

In the previous two subsections, we showed from the numerical simulations that whether magnetic fields are present or not, disks with Q smaller than a critical value can form gravitationally bound structures, while perturbations in relatively large- Q disks do not grow enough to produce a gravitational runaway. We also showed that gravitational runaways, when present, occur as a consequence of secondary instabilities working on the filaments or shearing wavelets that have already been amplified by MSAs. The secondary instabilities include three different processes: (1) immediate parallel fragmentation of filaments, (2) gravitationally-induced collisions of sheared patches, and (3) rejuvenated swing amplification. In this section we use specific examples to distinguish and illustrate each of the secondary instabilities.

Figure 15 compares the development of structure via the three different secondary instabilities. The left column in Figure 15 illustrates the parallel fragmentation process for model M05 (with $Q = 0.7$ and $\beta = 10$). The first frame of left column exhibits three filaments resulting from MSAs. The rightmost filament fragments into three discrete clumps (marked by square, triangle, and circle) at about $t/t_{\text{orb}} \sim 0.53$, while the leftmost filament with smaller surface density produces only one clump (marked by diamond) at $t/t_{\text{orb}} \sim 0.59$, as a result of the Jeans instability operating along the filaments. A relatively low-density clump condensed from the central filaments undergoes a collision with the remnant of the leftmost filament, becoming a very high-density entity after $t/t_{\text{orb}} \sim 0.65$. Elmegreen (1991) semi-analytically calculated growth factors for this parallel fragmentation instability and showed that they are very sensitive to Q and have a sharp threshold near $Q \sim 1$, which is in good agreement with the results of our simulations.

Collisionally-induced structure formation is exemplified in the center column of Figure 15, where we display four snapshots for model M07 (with $Q = 0.9$ and $\beta = 10$). A larger Q -value than in model M05 inhibits the parallel-fragmentation process discussed above, and thus model M07 still retains filamentary structure at $t/t_{\text{orb}} = 0.51$. Comparison of the first two frames in center column shows that k_x is almost unchanged during this time interval, indicating that the velocity fields are significantly modified from the initial values by both MSAs and gravitational interactions between the filaments; as a consequence, k_x does not secularly increase in time. Note that at $t/t_{\text{orb}} = 0.51$, $\Sigma_{\text{max}} \simeq 3\Sigma_0$ and $v_{x,\text{max}} \simeq 0.2v_{0,\text{max}}$, thus the radial motions of filaments are significant. The two filaments surrounded by boxes in the first frame are moving in radially opposite directions, and experience a physical collision with each other at $t/t_{\text{orb}} = 0.65$. The collision, accelerated by the mutual gravity between filaments, produces a new filament of higher density ($\Sigma \sim 5\Sigma_0$ at $t/t_{\text{orb}} = 0.80$). The central part of the newly born filament is in turn Jeans unstable, developing into a bound condensation, as marked by circle in the last frame of center column. Later, sheared patches further collide with each other to produce three more clumps ($t/t_{\text{orb}} > 1.19$). As we explained in §6.2, the presence of *weak* magnetic fields permits stronger post-collisional collapse by breaking potential vorticity conservation; *strong* magnetic fields could however inhibit physical collisions from taking place at all.

Finally, the right column of Figure 15 (see also Fig. 13) demonstrates how rejuvenated swing amplification develops for model M23 (with $Q = 1.1$ and $\beta = 1$). Since Q is relatively large, initial MSAs in model M10 do not amplify perturbations to the level where fragmentation or physical collisions of sheared filaments occur. Still, enhanced density is in the nonlinear regime, with $\Sigma_{\text{max}} \sim 1.3\Sigma_0$ when MSAs saturate. Individual wavelets tend to keep shearing out, but their nonlinear interactions restrain the shift to larger k_x of the overall power spectrum. At $t/t_{\text{orb}} = 1.59$, the maximum power of model M23 is achieved at $k_x = 7(2\pi/L)$, and $k_x \gtrsim 10(2\pi/L)$ modes have almost negligible power. Continued nonlinear interactions among shearing wavelets can feed fresh small- $|k_x|$ modes ($t/t_{\text{orb}} \sim 1.91$) that then undergo additional swing amplifications. Wavefronts of the principal “rejuvenated” swinging wavelets are indicated by dotted lines; these are not readily perceived until they grow significantly ($t/t_{\text{orb}} > 2.32$), because the power of these small- $|k_x|$ modes is initially small. Operating on an already nonlinear background, the rejuvenated swing amplification efficiently produces shearing patches of high surface density, especially when magnetic fields are present. The maximum surface density at $t/t_{\text{orb}} = 2.48$ is $\Sigma_{\text{max}} = 2.4\Sigma_0$. Overdense regions collect ambient material and suffer collisions with each other, finally to appear as bound condensations (see Fig. 12).

Although the above three types of the secondary instabilities are independent processes, in some cases they cooperate with each other to drive model disks into an ultimate gravitational runaway. For example, in models H07, M08, and M20, some fragmenting filaments undergo mutual collisions, while other filaments experience only parallel fragmentation. In models M09 and M21, on the other hand, gravitationally-induced collisions of sheared patches are not initially strong enough to produce immediate fragmentation, but high-power small- $|k_x|$ modes generated by the collisions

grow very rapidly as they swing around. Most generally, bound cloud formation may result from a combination of parallel fragmentation, physical collisions, and rejuvenated swing amplification, all of which work on sheared spiral wavelets previously amplified by MSAs.

6.4. Higher amplitude perturbations and other effects

In the preceding sections, we have presented simulations of the growth of structure from instabilities of low-amplitude ($\epsilon_0 = 10^{-3}$ or 10^{-2}) perturbations. Real galaxies, however, may have significantly larger perturbations.

One way to address this is by initiating simulations similar to those in §6.1-6.2, but with larger initial amplitudes. When we perform such simulations with $\epsilon_0 = 0.1$ and $\gamma = 1.5$, we find that the perturbations, aided by nonlinear effects acting from the outset of simulations, are so easily amplified that hydrodynamic disks with $Q \lesssim 1.2$ experience gravitational runaways within $\sim 0.4 t_{\text{orb}}$. The maximum surface density in larger- Q models also grows to a few times the mean density, but the background shear and the strong pressure gradients associated with both large Q values and the stiff equation of state ($\gamma = 1.5$) cause overdense regions in shearing wavelets to bounce back. Bouncing wavelets experience physical collisions with others moving in the opposite direction, but with high Q , bound condensations do not form. When we use an isothermal equation of state, on the other hand, there is essentially no pressure bounce for models with $Q \lesssim 1.9$, and overdense regions collapse in runaway fashion. Still, $Q \gtrsim 2$ models remain stable throughout the evolution. With magnetic fields included, we observe the similar evolutionary behavior to hydrodynamic cases, although magnetized collisions following pressure bounce form bound condensations more easily, and the critical values for the runaway collapse with $\gamma = 1$ are slightly smaller, giving $Q_c = 1.8 - 1.9$.

Does this imply that the critical Q values in real galaxies should be closer to 2 than the estimates in §6.1-6.2? We think not, because the initial conditions of the adopted power spectrum shape are unrealistic for actual large-amplitude perturbations. Perhaps more realistic “initial” conditions would be those occurring in the saturated intermediate state that develops from our low-amplitude simulations. These conditions are characterized by perturbations of amplitude $\sim 10 - 20\%$ of the background density, concentrated on radial scales $\sim 0.1 L$ (our model has $n_J = 5$, so from eq. [10] with typical parameters these scale are less than a kpc). For these intermediate states, we can measure the effective Q values for those models that lie at the boundary of susceptibility to secondary instabilities, taking allowance for the random perturbed velocity field, and modified local shear and local sound speed produced by the growth of perturbations. We find that the models (H11, M12, and M23) which show gravitational runaway have $Q_{\text{eff}} \leq 1.4$. The typical time required for the nonlinear interactions to produce the low- $|k_x|$ modes needed to seed the rejuvenated swing appears to be in the range of $\sim (1.5 - 2) t_{\text{orb}}$. Thus, we conclude that the critical values of Q to produce gravitational runaway from “natural” large-amplitude perturbations (other than spiral arms) are comparable to the critical values estimated in §§6.1, 6.2 to grow from small-amplitude perturbations.

A related issue concerns the detailed specification of the perturbations. For the simulations presented in this paper, we impose perturbations only on surface density, and initially kept the other variables uniform and constant. When evolved with an adiabatic equation of state, these isothermal perturbations give self-gravity a slight imbalance over the pressure gradient force, causing overdense regions to attract more material from the beginning of simulations. When we instead perturb both surface density and thermal energy in accordance with an isentropic initial condition, we find that the system undergoes an initial adjustment while trying to find the most unstable modes for MSAs. This relaxation stage involves a reduction of the density fluctuation amplitudes, sometimes affecting the destiny of the model’s dynamical evolution. For example, a model that has the same parameters as model M23 except initially isentropic perturbations experiences an initial decrease of density fluctuation amplitude by a factor of ~ 1.6 , and thus remains stable until the end of the simulation. Larger initial perturbation amplitudes lead to a larger “relaxation” reduction in fluctuating density amplitudes. This suggests that if isentropic rather than isothermal perturbations occur, then the critical Q values become slightly smaller. Equivalently, it implies that a slightly larger ϵ_0 is needed to induce secondary instabilities if perturbations are isentropic rather than isothermal. Because only models with already-marginal Q are subject to these differences, we do not consider the exact specification of initial conditions (except for their scale) crucial to the outcome.

7. Discussion

7.1. Summary of model results

In this paper, we have investigated both linear and nonlinear evolution of self-gravitational instabilities arising from nonaxisymmetric perturbations in local models of differentially rotating, magnetized, gaseous galactic disks. Our primary goals were to understand the parametric dependences of these instabilities, and to determine the conditions that ultimately lead to gravitational runaway. The disk models are infinitesimally thin, and we adopt an ideal gas equation of state with either an adiabatic or an isothermal pressure-density relation. We assume a uniform initial azimuthal magnetic field with $\beta = c_s^2/v_A^2$ (proportional to the gas-to-magnetic pressure ratio) characterizing the midplane field strength (see eq. [11]); we treat the magnetic field scale height as a constant in space and time. The local model we use incorporates the shear profile, tidal gravity, and Coriolis force arising from orbits in a smoothly-varying stellar + dark matter galactic gravitational potential, but does not include features such as stellar spiral arms. The relative importance of galactic rotational shear, self-gravity, and thermal pressure are described by the Toomre Q stability parameter (see eq. [7]) and the Jeans number n_J of the spatial scale under consideration (see eq. [8]). The background flow’s shear rate is measured by $q \equiv -d \ln \Omega / d \ln R$.

Our linear-theory analysis (§3) is aimed at exploring and delimiting the physical mechanisms for *initiating* self-gravitating condensations in two-dimensional disks. In §3.3, we employ the shearing-sheet formalism and integrate the resulting linearized equations over time. As long as $q \neq 0$, growth

of any linear perturbation eventually saturates owing to shear, so that a disturbance with a given (fixed) azimuthal wavelength can be characterized by the magnitude Γ of its total amplification over all time. We extensively analyze the dependence of the linear-theory saturated-state amplification on q , Q , and β .

Our linear analysis shows that there exist two distinct kinds of nonaxisymmetric instabilities (§3.3). Regions with weak shear ($q \ll 1$) and/or strong magnetic fields ($\beta \ll 1$) are susceptible to magneto-Jeans instabilities (MJI). For these modes (generalizations of those analyzed by Lynden-Bell (1966)), the presence of magnetic fields is essential for instability: tension forces transfer angular momentum, thereby greatly reducing the stabilizing effect of epicyclic motions. The stronger the magnetic fields, the more unstable low-shear regions become to nonaxisymmetric motions. On the other hand, when shear is relatively strong ($q \sim 1$) and the mean magnetic field moderate or weak ($\beta \gtrsim 1$), the growth of perturbations arises from magnetically-modified swing amplification (MSA), with a stabilizing role played by magnetic pressure. MSA is a generalization for MHD flows of the process originally studied by GLB. When $q \ll 1$, as needed for the MJI when galactic values of $\beta \gtrsim 1$ prevail, the slow increase of the local radial wavenumber gives disturbances plenty of time to attain huge amplification. When $q \sim 1$, as needed for the MSA, growth of perturbations is more moderate. The inclusion of magnetic fields lowers the amplification factor in the linear swing mechanism.

We also investigate the MJI using the coherent wavelet approach (§3.2), which allows us to obtain a closed-form dispersion relation (see eq. [23]), an instantaneous instability criterion (see eq. [24]), and approximate expressions for amplification magnitudes (see eqs. [26]). The amplification magnitudes obtained with this simplified approach agree well with the exact integrations of the linearized equations.

To determine the eventual fate of growing condensations – in particular, whether or not bound/collapsing clumps eventually form – we turn to numerical simulations. In our nonlinear evolution studies, we fix $n_J = 5$ for our standard simulation box (see eq. [10]) and allow q , Q , and β to vary so as to represent different disk models. Initially, we introduce small-amplitude density perturbations by adding either white noise (for MJI) or Gaussian random noise with a 2D Kolmogorov power spectrum (for MSA) and follow the time evolution of each disk model up to four orbital times.

In §5, we present the results of simulations with $q = 0.1$, corresponding to nonlinear evolution of MJI modes. With such low shear, perturbations grow almost exponentially to collapse within ~ 2 orbital times. The growth in the linear stage is predominantly along the mean field direction, and its rate is independent of the adiabatic index γ . When $\gamma \gtrsim 1.6$, thermal pressure halts the collapse and produces bound clumps.

In §6, we present the results of simulations with $q = 1$, i.e. flat rotation curves. These represent our study of the eventual outcomes from MSA. Because of the kinematic effects of shear, MSAs can grow for only a limited time before saturating at $t/t_{\text{orb}} \sim 0.7$ ($\sim 10^8$ yrs) (unless

strong nonlinear effects enter earlier). Disks with sufficiently small $Q < Q_c$ eventually collapse or form gravitationally bound clumps via nonlinear secondary instabilities (§6.3) operating on sheared spiral wavelets that have already been amplified by MSAs. These secondary instabilities include parallel fragmentation of filaments, gravitationally-induced collisions of nonlinear sheared patches, and “rejuvenated” swing amplification.

Which type of the secondary instability dominates depends on Q . In disks with $Q \lesssim 0.8$, parallel fragmentation instabilities dominate, while intermediate- Q disks ($Q \approx 0.9 - 1.0$ depending on β) preferentially exhibit collisionally-induced structure formation. When Q is slightly larger ($1.1 \lesssim Q < Q_c$ for $\beta \gtrsim 10$ or $1.0 \lesssim Q < Q_c$ for $\beta = 1$), the intermediate-state density enhancement from MSAs is too low to produce parallel fragmentation or physical collisions, but a second phase of swing amplification occurs. In “rejuvenated” swing, nonlinear interactions among sheared wavelets can supply fresh small- $|k_x|$ modes that then undergo sufficient swing amplification to produce gravitational runaway.

Our simulations show that embedded magnetic fields can strengthen nonlinear feedback, and accelerate post-collision collapse. The time required for structure formation tends to be shorter for lower Q , but for $Q > 1$, ultimate instability occurs not before 1.6 orbital times (4×10^8 yrs). The masses of collapsing regions or pressure-supported clumps are typically $\sim 10^7 M_\odot$.

Models with sufficiently large $Q > Q_c$ have low saturated-state density fluctuations and thus are not susceptible to secondary instability. We find that the critical values of Q that discriminate between the final outcomes, with gravitational runaway absent for $Q \geq Q_c$, are $Q_c = 1.3$ for $\beta = \infty$, $Q_c = 1.4$ for $\beta = 10$, and $Q_c = 1.2$ for $\beta = 1$, when the root mean square density fluctuations are initially $\epsilon_0 = 1\%$. These critical Q values are found to be insensitive to the simulation box size and the computational resolution, and slightly dependent (at a 10-20% level) on ϵ_0 and the adiabatic index γ .

As noted above, the computed values of Q_c from our nonlinear, nonaxisymmetric simulations are relatively insensitive to the magnetic field strength. In linear (nonaxisymmetric) theory, the corresponding result is the relatively weak dependence of the amplification magnitude for MSA on β (see Figs. 1-3). At the most basic level, this can be understood from the physics of linear swing amplification: most of the growth occurs during the “open spiral” phase of the swing ($k_x(t)$ near zero), when density ridges form near-radial spokes and the perturbed flow velocities are primarily azimuthal. Since the background magnetic fields are themselves azimuthal, flow in the open phase is nearly along field lines and hence relatively unaffected by magnetic forces. For comparison, *linear, axisymmetric* modes have instability thresholds at $Q_c = (1 + \beta^{-1})^{-1/2}$, or 1, 0.95, and 0.71 for $\beta = \infty$, 10, and 1, respectively. Our finding that the nonlinear, nonaxisymmetric Q_c is smallest for $\beta = 1$ may reflect the reduction in amplification by radial magnetic pressure gradients during the more strongly leading/trailing phases of the swing. Our finding that the nonlinear, nonaxisymmetric Q_c is larger for $\beta = 10$ than for $\beta = \infty$ is indicative of the role magnetic fields play in “rejuvenating” swing by enhancing feedback to low- k_x modes. We note that this result

could not have been predicted solely from the linear analysis: Figure 2 shows that the amplification magnitude Γ increases with increasing β , for linear MSA.

7.2. Application to inner galaxies

One of the most interesting results of our study is seeing how magnetic fields dramatically alter dynamics in a weak-shear environment. The underlying physical reason for this is that magnetic tension reduces the stabilizing effect from Coriolis forces, and thus in the limiting case of very strong fields makes shear instability essentially the same as the 2D Jeans instability in the azimuthal direction (cf. Elmegreen (1987a)). This MJI could, at least partly, explain the active star formation observed towards the central parts of galaxies where rotation curves are nearly solid body and the star formation rate is generally orders of magnitude higher than in outer disks (e.g., Kennicutt (1998)). Nuclear starburst activity – or even bulge formation in a dark matter halo without a central cusp – may represent the extreme of this phenomenon.

Other physical processes that might influence the nuclear star-formation activity include molecular gas content, external disturbances from nearby or interacting galaxies, and nuclear gas transport via inner Lindblad resonance and bars (cf. Jogee (2000)). However, there is intriguing evidence that starburst activity is closely linked to the slope of the rotation curve. For example, the starburst galaxy M82 has vigorous star formation in the rigidly rotating part, and weak star formation beyond the turnover point of the rotation curve (Telesco et al 1991). Kenney et al (1993) also found that the starburst region in NGC 3504 corresponds to the linearly rising portion of the rotation curve. Kenney et al (1993) estimated Q near 0.9 for the center of this galaxy, which does not rule out the possibility of axisymmetric gravitational instability provided $\beta > 4$. The corresponding growth time for axisymmetric modes is $\zeta^{-1} \sim \Omega^{-1}$ from equation (23) with $\beta = \infty$. On the other hand, if there are significant embedded magnetic fields ($\beta < 4$) in the azimuthal direction that preclude *axisymmetric* instabilities, then *nonaxisymmetric* MJIs can account for the growth of gas complexes. The coherent wavelet solution (23) yields the growth time for nonaxisymmetric modes of $\tau_{\text{grow}} \equiv \zeta_{\text{max}}^{-1} = (0.5 - 0.7) \Omega^{-1}$ for $Q = 0.9$, $q = 0$, and $\beta = 1 - 10$ (with higher β giving larger τ_{grow}). For $\Omega \sim (500 - 1000) \text{ km s}^{-1} \text{ kpc}^{-1}$ observed in the central few hundred parsecs of NGC 3504, this amounts to $\sim (5 - 14) \times 10^5$ yrs.

MJIs could also potentially explain the vigorous star formation activity near the inner regions of the late-type spiral galaxies M33 and NGC 2403, where rotation curves are rising slowly with radius. Kennicutt (1989) and Martin & Kennicutt (2001) found that the inner parts of both galaxies have gas surface densities well below the minimum required to meet the Q -threshold criterion empirically determined from outer-galaxy star formation. Martin & Kennicutt (2001) suggest, however, that if one applies an alternative criterion for instability in weak-shear regions proposed by Elmegreen (1993b) and Hunter, Elmegreen, & Baker (1998) for irregular galaxies, the star formation in the interiors of M33 and NGC 2403 can be explained. Here, we relate to and generalize this “shear criterion” based on our results for MJI.

Similarly to Elmegreen (1993b), we posit that instability significant enough to produce active star formation corresponds to sufficient total growth of the MJI before shear causes saturation. With Γ_{\max} the log of the total amplification of linear perturbations, $\Gamma_{\max} > \Gamma_c$ for some Γ_c thus defines an instability threshold. If magnetic fields are very strong, $((c_s/v_A)^2 \equiv \beta \ll 1)$, growth at the Jeans rate $\approx \pi G \Sigma / c_s$ persists for a time $(q\Omega)^{-1}$. Equation (26a) would thus imply instability when

$$Q_A \equiv \frac{q\Gamma_c Q}{2\sqrt{1-q/2}} = \frac{2\Gamma_c A c_s}{\pi G \Sigma_0} < 1, \quad \text{for } \beta \ll 1, \quad (28)$$

where $A \equiv q\Omega/2$ is Oort’s shear parameter. The shear criterion of Elmegreen (1993b) corresponds to equation (28) with $\Gamma_c = 1.25$.

When magnetic fields are moderate or weak ($c_s/v_A \gtrsim 1$), the MJI growth rate is reduced below the Jeans rate, and our equation (26b) would then imply instability for weak-shear regions where $q \lesssim 0.7\beta^{-1/3}Q^{-1}$ provided

$$Q_w \equiv \left(\frac{q\Gamma_c c_s}{1.6v_A} \right)^{1/2} Q < 1. \quad (29)$$

Our *nonlinear* simulations of the MSA indicate that the threshold for gravitational runaway occurs at Q such that Γ for *linear* wavelets would be near unity (see Tables 1,2). If the critical amplification Γ_c for MJI is similar, then equation (29) would predict instability provided $(qc_s/v_A)^{1/2}Q \lesssim 1.3$. The threshold surface density from equation (29) is generally larger than from equation (28), but smaller than would nominally be required for MSA (which however *cannot* occur in low-shear regions). In particular, if we use the observational parameters for NGC 2403 from Martin & Kennicutt (2001), instability under the condition (29) with $\Gamma_c \gtrsim 1$ is predicted only in the very innermost regions; to have instability over the whole inner region would require $\Gamma_c < 1$. Since $\Gamma < 1$ would correspond to relatively weak growth of perturbations, it seems likely that instead either the steep part of the rotation curve extends to larger radius than presently estimated (current measures suffer from low resolution) – allowing $\Gamma_c \gtrsim 1$, or that effects from spiral arms are important for explaining the high star formation rate in much of the inner portion of this galaxy.

7.3. Application to outer galaxies

Since the bulk of disk material in spiral galaxies orbits following a flat rotation profile (e.g., Sofue et al (1999)), $q \sim 1$ is a good representation for local shear outside of the central regions. Magnetic fields in spiral galaxies have a mean field component of typically a few μG (Beck et al 1996), corresponding to $\beta \sim 1$ to 10. Therefore, MSA modes are probably more important than MJI modes in initiating the growth of self-gravitating structures in extended disks of spiral galaxies – *outside* of lowered-shear spiral arms.

The two main characteristics of linear MSA modes are the limit to initial growth of imposed perturbations from the shearing of wave crests, and the stabilizing effects of embedded magnetic fields. Our numerical simulations show that if Q is not less than unity and initial multi-kpc scale

perturbations are $\sim 1\%$, the density enhancement at $t \sim 10^8$ yrs, when MSAs are fully developed and kinematically saturated, is not large enough to produce gravitationally bound structures. The presence of magnetic fields reduces the growth of density perturbations by MSA even further, so that when $\beta = 1$, only $Q \lesssim 0.8$ models can achieve sufficient density to collapse right away. Although subsequent nonlinear interactions among shearing wavelets could give an extra boost for $1 \lesssim Q \lesssim 1.4$, leading to the formation of bound condensations, the whole process takes more than $\sim 4 \times 10^8 - 10^9$ yrs, longer than the available timescale of 10^8 yrs for the growth of perturbations without being disturbed by random supernova events, formation of OB associations, and larger-scale density waves (Elmegreen 1987a, 1993a). This suggests that MSAs in disks can produce observed GMAs or HI superclouds in spiral galaxies where shear is relatively high and Q is large, only with the aid of additional agents. We discuss some potential additional effects below.

In this study, we idealized the multiphase gaseous medium using inviscid monolayers, so that our model disks do not incorporate the destabilizing effect of viscosity potentially associated with mutual collisions of cloudlets having large mean free paths (cf. Gammie (1996)). By making a thin-disk approximation, our model disks overestimate the self-gravity at the disk midplane (cf. Toomre (1964)); a correction for finite thickness would decrease the critical Q -values. A more significant drawback associated with the simplified geometry is that 2D simulation models cannot capture the potential consequences of magnetorotational instabilities (MRIs; e.g., Balbus & Hawley (1998)) and the Parker instability (Parker 1966) on cloud formation. MRIs, which exist only in 3D systems, are known to generate MHD turbulence in accretion disks and may also contribute to large-scale turbulence in galactic disks (Sellwood & Balbus 1999). Because gravitational instabilities in outer disks are primarily limited by shear, and MRIs require weak enough magnetic fields that shear is not significantly suppressed, MRIs may primarily affect growth timescales rather than Q thresholds. Parker instability has often been invoked in the formation of molecular clouds along spiral arms where shear is reduced (e.g., Blitz & Shu (1980); see discussion in Elmegreen (1995a) and references therein). Outside of spiral arms, the primary role of Parker instability might be in helping to seed large-scale perturbations which then become self-gravitating via MSA. To understand the full dynamical impact of these instabilities combined with self-gravity, it is desirable to expand the current work into 3D, also making allowance for a multiphase ISM.

In the present study, we considered structure formation only in a gaseous component and followed its linear and nonlinear evolution under its own gravity. Real galaxies, of course, consist of both gaseous and stellar disks. Although the velocity dispersion of stars is larger than the gas sound speed typically by an order of magnitude, the contribution of the stellar part to the dynamical evolution of the combined system for axisymmetric linear modes is almost comparable to that of the gaseous part if the gas fraction is $\sim 10 - 25\%$ (Jog & Solomon 1984a). Elmegreen (1995b) and Jog (1996) extended the work of Jog & Solomon (1984a) and showed that the gravitational coupling of these two components makes the combined two-fluid system more unstable than each disk alone. Jog (1992) studied nonaxisymmetric swing amplification in a two-fluid system and found that unlike the situation for axisymmetric instability (in which gas and stars respond coherently with the same

growth rates), the lower velocity dispersion of the gas in the nonaxisymmetric instability allows for a larger amplification in gas than in stars. More extensive study of the effect of a “live” stellar component on the linear and nonlinear outcome of MSA in a gaseous disk represents an important direction for future research. Qualitatively, it is clear that the inclusion of stellar gravity would tend to increase the critical Q values and shorten the time for the instability to form gravitationally bound objects.

While the linear theory yields MSA amplification factors that vary continuously with respect to Q , our numerical simulations show that a small change in Q near the critical value results in dramatically different final states, owing to nonlinear interactions of shearing wavelets. The evidence for critical Q values in deciding the outcome of the nonaxisymmetric instabilities is suggestive of the observationally-inferred threshold for determining global star formation in spiral galaxies. Although bound structures may take some time to form, the critical values ($Q_c \sim 1.2 - 1.4$ depending on β) obtained from our simulations are similar to the observational threshold value $Q_c \sim 1.4$ very recently reported by Martin & Kennicutt (2001). This quantitative agreement is certainly encouraging, but of greater importance is simply the concrete demonstration that disks which are linearly stable ($Q > 1$) nevertheless show robust threshold behavior for self-gravitational runaway under a variety of conditions – as anticipated by empirical models.

The empirical threshold model predicts radial trends in star formation by employing azimuthally-averaged gas surface densities and rotation curves, while in fact azimuthal variations of gas surface densities and the shear rate due to gas streaming motions are substantial. Given the strong spatial association of giant cloud complexes and active star formation with spiral density waves, the azimuthally-averaged star formation threshold model is evidently oversimplified. A straightforward extension of the “axisymmetric” star formation threshold model would be to take account of spiral structure, with active star formation at some radius expected provided that the local value of Q within arms at that radius is smaller than some threshold. This extension tends to bring observed thresholds closer to our estimates and also reduces growth timescales, as we explain next.

Long-lived global spiral density waves (Lin & Shu 1964, 1966) may have a dramatic effect on small-scale structure formation, because the enhanced density in wave crests makes the local Q value and shear rate smaller than in the interarm regions. In the hydrodynamic theory, $Q_s = Q_0(\Sigma_s/\Sigma_0)^{-0.5}$ for an isothermal gas, and the local shear gradient is $q_s = 2 - (2 - q)\Sigma_s/\Sigma_0$, where the “s” and “0” subscripts denote respectively arm and interarm values (Balbus & Cowie 1985; Elmegreen 1994). These scalings suggest that it would not be difficult to obtain $Q_s \lesssim 0.7$ and $q_s \sim 0$ for typical arm-interarm contrasts of a few to several in spiral galaxies. Naive application of our present analyses to spiral arm crests with such small Q and q local conditions suggests that collapse of arm gas could proceed very rapidly via MJI modes, forming condensations within one Jeans time scale (a few times 10^7 yrs). The observed strong association of giant cloud complexes with spiral arms (e.g., Kenney (1997)) supports the idea of their triggered formation mechanism by spiral density waves. GMAs even in flocculent galaxies appear to be associated with weak, near-infrared arms (e.g., Thornley & Mundy (1997a,b)).

Although the above extrapolations of (unmagnetized) linear theory and indications from observations are highly suggestive, the detailed nonlinear MHD evolution within arms has yet to be explored theoretically. Linear analysis suggests that additional stabilizing and destabilizing terms may be important when the background has large density variations; i.e., a strong arm (Balbus 1988). It is unknown, however, how the epicycle frequency (or, equivalently local shear rate) varies inside arms when the conservation of the potential vorticity is broken due to magnetic fields. Do phase correlations of the background density and velocity gradients in the arm still determine the character of instabilities, as suggested by Balbus (1988) when $B = 0$? Numerical computations with explicit inclusion of spiral arm potentials are required to address these and related questions, extending the effort to understand the highly complex problem of cloud and star formation in spiral galaxies.

We gratefully acknowledge J. M. Stone for providing the original ZEUS 2D code and many helpful insights, and are thankful to C. F. Gammie for sharing his shearing-sheet Poisson solver and expert comments on the manuscript. We also thank S. Vogel and B. Elmegreen for constructive comments, and are grateful to an anonymous referee for a detailed and insightful report. This work was supported by NASA grants NAG 53840 and NAG 59167.

REFERENCES

- Balbus, S. A. 1988, *ApJ*, 324, 60
- Balbus, S. A., & Cowie, L. L. 1985, *ApJ*, 297, 61
- Balbus, S. A., & Hawley, J. F. 1998, *Rev. Mod. Phys.*, 70, 1
- Balbus, S. A., & Papaloizou, J. C. 1999, *ApJ*, 521, 650
- Beck, R., Brandenburg, A., Moss, D., Shukurov, A., & Sokoloff, D. 1996, *ARA&A*, 34, 155
- Binney, J., & Tremaine, S. 1987, *Galactic Dynamics* (Princeton: Princeton Univ. Press)
- Blitz, L., & Shu, F. H. *ApJ*, 238, 148
- Chandrasekhar, S. 1954, *ApJ*, 119, 7
- Cohen, R. S., Grabelsky, D. A., May, J., Bronfman, L., Alvarez, H., & Thaddeus, P. 1985, *ApJ*, 290, L15
- Crutcher, R. M. 1999, *ApJ*, 520, 706
- Dame, T. M. 1993, in *Back to the Galaxy*, eds. S. Holt & F. Verter (AIP: New York), 267
- Dickey, J. M., & Lockman, F. J. 1990, *ARA&A*, 28, 215

- Dwarkadas, V. V., & Balbus, S. A. 1996, *ApJ*, 467, 87
- Elmegreen, B. G. 1979, *ApJ*, 231, 372
- Elmegreen, B. G. 1987a, *ApJ*, 312, 626
- Elmegreen, B. G. 1987b, in *IAU Symposium 115: Star Forming Regions*, eds. M. Peimbert & J. Jugaku (Dordrecht: Reidel), 457
- Elmegreen, B. G. 1991, *ApJ*, 378, 139
- Elmegreen, B. G. 1992, in *Star Formation in Stellar Systems*, eds. G. Tenorio-Tagle, M. Prieto, & F. Sanchez, (Cambridge: Cambridge University Press), 381
- Elmegreen, B. G. 1993a, in *Protostars and Planets III*, eds. E. Levy & J. Lunine (Tucson:University of Arizona Press), 97
- Elmegreen, B. G. 1993b, in *Star Formation, Galaxies and the Interstellar Medium*, eds. J. Franco, F. Ferrini, & G. Tenorio-Tagle (Cambridge:Cambridge Univ. Press), 337
- Elmegreen, B. G. 1994, *ApJ*, 433, 39
- Elmegreen, B. G. 1995a, in *The 7th Guo Shoujing Summer School on Astrophysics: Molecular Clouds and Star Formation*, eds. C. Yuan & Hunhan You (Singapore:World Scientific), 149
- Elmegreen, B. G. 1995b, *MNRAS*, 275, 944
- Elmegreen, B. G. 1996, in *IAU Symposium 169: Unsolved Problems of the Milky Way*, eds. L. Blitz & P. Teuben (Dordrecht:Kluwer), 551
- Elmegreen, B. G., & Elmegreen, D. M. 1983, *MNRAS*, 203, 31
- Evans, C. R., & Hawley, J. F. 1988, *ApJ*, 332, 659
- Fan, Z. H., & Lou, Y.-Q. 1997, *MNRAS*, 291, 91
- Gammie, C. F. 1992, Ph.D. Thesis, Princeton University
- Gammie, C. F. 1996, *ApJ*, 462, 725
- Gammie, C. F. 2001, *ApJ*, accepted
- Goldreich, P., & Lynden-Bell, D. 1965, *MNRAS*, 130, 125 (GLB)
- Grabelsky, D. A., Cohen, R. S., Bronfman, L., Thaddeus, P., & May, J. 1987, *ApJ*, 315, 122
- Hawley, J. F., Gammie, C. F., & Balbus, S. A. 1995, *ApJ*, 440, 742
- Hawley, J. F., & Stone, J. M. 1995, *Comput. Phys. Commus.*, 89, 127

- Heiles, C. 2000, in Fourth Tetons Conference: Galactic Structure, Stars, and the Interstellar Medium, eds. M. D. Bica & C. E. Woodward (ASP Press: San Francisco); astro-ph/0010047
- Hunter, C. 1964, *ApJ*, 139, 570
- Hunter, D. A., Elmegreen, B. G., & Baker, A. L. 1998, *ApJ*, 493, 595
- Jog, C. 1992, *ApJ*, 390, 378
- Jog, C. 1996, *MNRAS*, 278, 209
- Jog, C., & Solomon, P. M. 1984a, *ApJ*, 276, 114
- Jog, C., & Solomon, P. M. 1984b, *ApJ*, 276, 127
- Jogee, S. 2000, in IAU Symposium 205: Galaxies and their Constituents at the Highest Angular Resolution, eds. R. T. Schilizzi, S. Vogel, F. Paresce, & M. Elvis (Manchester: ASP), 29
- Julian, W. H., & Toomre, A. 1966, *ApJ*, 146, 810 (JT)
- Kenney, J. D. P., Carlstrom, J. E., & Young, J. S. 1993, *ApJ*, 418, 687
- Kenney, J. D. P. 1997, in *The Interstellar Medium in Galaxies*, ed. J. M. van der Hulst (Dordrecht:Kluwer), 33
- Kennicutt, R. C. 1989, *ApJ*, 344, 685
- Kennicutt, R. C. 1997, in *The Interstellar Medium in Galaxies*, ed. J. M. van der Hulst (Dordrecht:Kluwer), 171
- Kennicutt, R. C. 1998, *ARA&A*, 36, 189
- Kim, W.-T., & Ostriker, E. C. 2000, *ApJ*, 540, 372
- Knapen, J. H., Cepa, J., Beckman, J. E., Soledad del Rio, M., & Pedlar, A. 1993, *ApJ*, 416, 563
- Kulkarni, S. R., & Heiles, C. 1987, in *Interstellar Processes*, eds. D.J. Hollenbach & H.A. Thronson (Dordrecht:Reidel), 87
- Lin, C. C., & Shu, F. H. 1964, *ApJ*, 140, 646
- Lin, C. C., & Shu, F. H. 1966, *Proc. Nat. Acad. Sci.*, 55, 229
- Lin, C. C., & Shu, F. H. 1971, in *Astrophysics and General Relativity*, eds. M. Chretien, S. Deser, & J. Goldstein (New York: Gordon & Breach), 2:236
- Lou, Y.-Q., & Fan, Z. H. 1998, *ApJ*, 493, 102
- Lynden-Bell, D. 1966, *Observatory*, 86, 57

- Martin, C. L., & Kennicutt, R. C. 2001, ApJ, accepted; astro-ph/0103181
- Masset, F. 2000, A&AS, 141, 165
- Myers, P. C., & Goodman, A. A. 1988a, ApJ, 326, L27
- Myers, P. C., & Goodman, A. A. 1988b, ApJ, 329, 392
- Ostriker, E. C., Shu, F. H., & Adams, F. C. 1992, ApJ, 399, 192
- Parker, E. N. 1966, ApJ, 145, 811
- Quirk, W. J. 1972, ApJ, 176, L9
- Rand, R. J. 1993, ApJ, 410, 68
- Rand, R. J., & Kulkarni, S. R. 1990, ApJ, 349, L43
- Rand, R. J., & Lyne, A. G. 1994, MNRAS, 268, 497
- Ryu, D., & Goodman, J. 1992, ApJ, 388, 438
- Safronov, V. S. 1960, Ann. d’Astrophys., 23, 979
- Sakamoto, K. 1996, ApJ, 471, 173
- Sakamoto, K., Okumura, S. K., Ishizuki, S., & Scoville, N. Z. 1999, ApJS, 124, 403
- Sellwood, J. A., & Balbus, S. A. 1999, ApJ, 511, 660
- Shu, F. H. 1974, A&A, 33, 55
- Shu, F. H. 1992, The Physics of Astrophysics. II. Gas Dynamics (Mill Valley: Univ. Science Books)
- Sofue, Y., Tutui, Y., Honma, M., Tomita, A., Takamiya, T., Koda, J., & Takeda, Y. 1999, ApJ, 523, 136
- Solomon, P. M., Sanders, D. B., & Rivolo, A. R. 1985, ApJ, 292, L19
- Stark, A. A. 1979, Ph.D. Thesis, Princeton University
- Stone, J. M., & Norman, M. L. 1992a, ApJS, 80, 753
- Stone, J. M., & Norman, M. L. 1992b, ApJS, 80, 791
- Taylor, C. L., Brinks, E., Pogge, R. W., & Skillman, E. D. 1994, AJ, 107, 971
- Telesco, C. M., Campins, H., Joy, M., Dietz, K., & Decher, R. 1991, ApJ, 369, 135
- Thornley, M. D., & Mundy, L. G. 1997a, ApJ, 484, 202

- Thornley, M. D., & Mundy, L. G. 1997b, *ApJ*, 490, 682
- Toomre, A. 1964, *ApJ*, 139, 1217
- Toomre, A. 1981, in *Structure and Evolution of Normal Galaxies*, eds. S. M. Fall & D. Lynden-Bell (Cambridge:Cambridge Univ. Press), 111
- Truelove, J. K., Klein, R. I., McKee, C. F., Holliman, J. H., II, Howell, L. H., & Greenough, J. A. 1997, *ApJ*, 489, L179
- Truelove, J. K., Klein, R. I., McKee, C. F., Holliman, J. H., II, Howell, L. H., Greenough, J. A., & Woods, D. T. 1998, *ApJ*, 495, 821
- van der Hulst, J. M., Skillman, E. D., Smith, T. R., Bothun, G. D., McGaugh, S. S., & de Blok, W. J. G. 1993, *AJ*, 106, 548
- Vogel, S. N., Kulkarni, S. R., & Scoville, N. Z. 1988, *Nature*, 334, 402
- Williams, J. P., Blitz, L., & McKee, C. F. 2000, in *Protostars and Planets IV*, eds. Mannings, Boss, & Russell (Tuscon:Univ. of Arizona press), 97
- Young, J. S., & Scoville, N. Z. 1991, *ARA&A*, 29, 581

Table 1. Parameters of Hydrodynamic Simulations with Strong Shear.

Model (1)	Q (2)	n_J (3)	γ (4)	ϵ_0 (5)	Grid (6)	$\tau_{1st}^{a,b,c}$ (7)	$\Gamma_{1st}^{c,d}$ (8)	τ_{2nd}^b (9)	Result (10)
H01	0.9	5	1.5	10^{-3}	256×256	0.88(0.87)	2.36(2.30)	0.8	Unstable
H02	1.0	5	1.5	10^{-3}	256×256	0.79(0.78)	1.95(1.95)	2.0	Unstable
H03	1.1	5	1.5	10^{-3}	256×256	0.72(0.71)	1.63(1.63)	>4	Stable
H04	1.2	5	1.5	10^{-3}	256×256	0.70(0.65)	1.38(1.38)	>4	Stable
H05	1.3	5	1.5	10^{-3}	256×256	0.65(0.60)	1.18(1.19)	>4	Stable
H06	0.7	5	1.5	10^{-2}	256×256(1.11)(3.35)	0.5	Unstable
H07	0.8	5	1.5	10^{-2}	256×256(0.97)(2.75)	0.6	Unstable
H08	0.9	5	1.5	10^{-2}	256×256	0.82(0.87)	1.99(2.30)	0.7	Unstable
H09	1.0	5	1.5	10^{-2}	256×256	0.78(0.78)	1.85(1.95)	1.1	Unstable
H10	1.1	5	1.5	10^{-2}	256×256	0.76(0.71)	1.61(1.63)	1.9	Marginal
H11	1.2	5	1.5	10^{-2}	256×256	0.69(0.65)	1.37(1.38)	2.1	Marginal
H12	1.3	5	1.5	10^{-2}	256×256	0.65(0.60)	1.18(1.19)	>4	Stable
H13	1.4	5	1.5	10^{-2}	256×256	0.58(0.56)	1.04(1.03)	>4	Stable
H14	1.0	5	1.0	10^{-2}	256×256(0.78)(1.95)	0.6	Unstable
H15	1.2	5	1.0	10^{-2}	256×256	0.70(0.65)	1.40(1.38)	1.9	Unstable
H16	1.3	5	1.0	10^{-2}	256×256	0.65(0.60)	1.20(1.19)	>4	Stable
H17	1.4	5	1.0	10^{-2}	256×256	0.58(0.56)	1.05(0.03)	>4	Stable
H18	1.0	5	2.0	10^{-2}	256×256	0.76(0.78)	1.78(1.95)	1.1	Marginal
H19	1.2	5	2.0	10^{-2}	256×256	0.69(0.65)	1.36(1.38)	2.1	Marginal
H20	1.0	10	1.5	10^{-2}	256×256	0.71(0.78)	1.84(1.95)	1.1	Unstable
H21	1.2	10	1.5	10^{-2}	256×256	0.69(0.65)	1.40(1.38)	2.1	Stable
H22	1.2	5	1.5	10^{-2}	512×512	0.69(0.65)	1.37(1.38)	2.1	Marginal
H23	1.2	5	1.5	10^{-2}	128×128	0.69(0.65)	1.36(1.38)	2.1	Marginal

^adefined by the time at which $\epsilon \equiv (\Sigma/\Sigma_0 - 1)^2 >^{1/2}$ attains its first maximum

^bin the unit of the orbital period t_{orb}

^cthe values in the parentheses are from the linear analyses with $K_y = 0.2$.

^d $\Gamma_{1st} = \log[\epsilon(\tau_{1st})/\epsilon_0] = \frac{1}{2} \log[< (\Sigma - \Sigma_0)^2 >_{\tau_{1st}} / < (\Sigma - \Sigma_0)^2 >_0]$

Table 2. Parameters of Magnetohydrodynamic Simulations with Strong Shear.

Model (1)	β (2)	Q (3)	n_J (4)	γ (5)	ϵ_0 (6)	$\tau_{1st}^{a,b,c}$ (7)	$\Gamma_{1st}^{c,d}$ (8)	τ_{2nd}^b (9)	Result (10)
M01	10	1.0	5	1.5	10^{-3}	0.75(0.78)	1.76(1.69)	2.4	Unstable
M02	10	1.1	5	1.5	10^{-3}	0.72(0.73)	1.48(1.42)	3.4	Marginal
M03	10	1.2	5	1.5	10^{-3}	0.65(0.65)	1.26(1.21)	>4	Stable
M04	10	1.3	5	1.5	10^{-3}	0.59(0.55)	1.10(1.05)	>4	Stable
M05	10	0.7	5	1.5	10^{-2}(1.11)(2.96)	0.5	Unstable
M06	10	0.8	5	1.5	10^{-2}(0.97)(2.44)	0.6	Unstable
M07	10	0.9	5	1.5	10^{-2}	0.71(0.86)	1.87(2.02)	0.9	Unstable
M08	10	1.0	5	1.5	10^{-2}	0.74(0.78)	1.70(1.69)	1.1	Unstable
M09	10	1.1	5	1.5	10^{-2}	0.72(0.73)	1.46(1.42)	1.7	Unstable
M10	10	1.2	5	1.5	10^{-2}	0.64(0.65)	1.26(1.21)	2.1	Unstable
M11	10	1.3	5	1.5	10^{-2}	0.59(0.55)	1.10(1.05)	2.5	Unstable
M12	10	1.4	5	1.5	10^{-2}	0.58(0.54)	0.97(0.91)	3.2	Marginal
M13	10	1.5	5	1.5	10^{-2}	0.57(0.52)	0.87(0.81)	>4	Stable
M14	10	1.6	5	1.5	10^{-2}	0.56(0.49)	0.78(0.72)	>4	Stable
M15	1	0.8	5	1.5	10^{-3}	0.52(0.59)	1.46(1.42)	1.4	Unstable
M16	1	0.9	5	1.5	10^{-3}	0.50(0.51)	1.26(1.23)	3.5	Marginal
M17	1	1.0	5	1.5	10^{-3}	0.48(0.48)	1.09(1.07)	>4	Stable
M18	1	1.1	5	1.5	10^{-3}	0.48(0.47)	0.95(0.95)	>4	Stable
M19	1	0.7	5	1.5	10^{-2}(0.69)(1.68)	0.6	Unstable
M20	1	0.8	5	1.5	10^{-2}(0.59)(1.42)	0.8	Unstable
M21	1	0.9	5	1.5	10^{-2}	0.54(0.51)	1.27(1.23)	1.2	Unstable
M22	1	1.0	5	1.5	10^{-2}	0.50(0.48)	1.10(1.07)	1.4	Unstable
M23	1	1.1	5	1.5	10^{-2}	0.48(0.47)	0.97(0.95)	2.3	Unstable
M24	1	1.2	5	1.5	10^{-2}	0.47(0.46)	0.87(0.85)	>4	Stable
M25	1	1.3	5	1.5	10^{-2}	0.46(0.45)	0.78(0.76)	>4	Stable
M26	1	1.4	5	1.5	10^{-2}	0.46(0.44)	0.71(0.69)	>4	Stable
M27	1	1.0	5	1.0	10^{-2}	0.50(0.48)	1.10(1.07)	1.0	Unstable
M28	1	1.1	5	1.0	10^{-2}	0.48(0.47)	0.97(0.95)	2.3	Unstable

Table 2—Continued

Model (1)	β (2)	Q (3)	n_J (4)	γ (5)	ϵ_0 (6)	$\tau_{1st}^{a,b,c}$ (7)	$\Gamma_{1st}^{c,d}$ (8)	τ_{2nd}^b (9)	Result (10)
M29	1	1.2	5	1.0	10^{-2}	0.47(0.46)	0.87(0.85)	>4	Stable
M30	1	1.0	5	2.0	10^{-2}	0.50(0.47)	1.09(1.07)	>4	Unstable
M31	1	1.0	10	1.5	10^{-2}	0.51(0.48)	1.14(1.07)	1.3	Unstable
M32	1	1.1	10	1.5	10^{-2}	0.49(0.47)	0.99(0.95)	2.1	Unstable
M33	1	1.2	10	1.5	10^{-2}	0.48(0.46)	0.87(0.85)	3.7	Stable
M34	1	1.3	10	1.5	10^{-2}	0.47(0.45)	0.80(0.76)	>4	Stable
M35 ^e	1	1.0	5	1.5	10^{-2}	0.49(0.48)	1.14(1.07)	1.4	Unstable
M36 ^e	1	1.1	5	1.5	10^{-2}	0.48(0.47)	0.99(0.95)	2.4	Unstable
M37 ^e	1	1.2	5	1.5	10^{-2}	0.47(0.46)	0.89(0.85)	>4	Stable
M38 ^e	1	1.3	5	1.5	10^{-2}	0.46(0.45)	0.81(0.76)	>4	Stable

^adefined by the time at which $\epsilon \equiv < (\Sigma/\Sigma_0 - 1)^2 >^{1/2}$ attains its first maximum

^bin the unit of the orbital period t_{orb}

^cthe values in the parentheses are from the linear analyses with $K_y = 0.2$.

^d $\Gamma_{1st} = \log[\epsilon(\tau_{1st})/\epsilon_0] = \frac{1}{2} \log[< (\Sigma - \Sigma_0)^2 >_{\tau_{1st}} / < (\Sigma - \Sigma_0)^2 >_0]$

^e2D Burgers spectrum is used to generate initial density perturbations

Fig. 1.— Total amplification magnitude Γ of linear gravitational instabilities in a thin shearing disk with an embedded azimuthal magnetic field. $Q = 1.3$ and $K_y \equiv k_y/k_J = 0.5$ are adopted. Solid lines are drawn from the direct numerical integration of the linearized shearing sheet equations, while dotted lines are the results of the coherent wavelet solutions; when $q \ll 1$ or $\beta \ll 1$, corresponding to the condition for MJJ, these two results are in good agreement with each other. For $0.6 < q < 2$ and $\beta \gtrsim 1$, MSA prevails, with solutions following the unmagnetized swing amplification result (heavy curve).

Fig. 2.— Parametric dependence on Q and β of total linear-theory amplification magnitude Γ for the case of $K_y = 0.2$ and $q = 1$. The numbers labeling heavy contours correspond to Γ . The interval of the light contours is given by $\Delta\Gamma = 0.1$. The discontinuity in Γ at $\beta_c \sim 0.1 - 1$ is indicative of the two different mechanisms responsible for instabilities: MJJ for $\beta < \beta_c$ and MSA for $\beta > \beta_c$. See text for details.

Fig. 3.— Total linear-theory amplification magnitude Γ as a function of the dimensionless azimuthal wavenumber $K_y \equiv k_y/k_J$. For $\beta \gtrsim 1$, Γ peaks at $K_y \sim 0.15 - 0.4$ with smaller- and larger- K_y regions stabilized by epicyclic motion and MHD waves, respectively. For $\beta \ll 1$, stabilization by the epicyclic motion occurs at $K_y \lesssim 0.1\beta$. Discontinuities in $\beta = 1$ curves show that MSA (MJJ) applies for smaller (larger) K_y modes.

Fig. 4.— A test run with a 128×128 resolution for MSA of a single nonaxisymmetric mode. Solid lines obtained from the numerical simulation are in good agreement with open circles taken from the results of linear analysis. $Q = 2$, $n_J = 2.5$, $q = 1$, $\gamma = 1.5$, and $\beta = 1$ are adopted and sinusoidal perturbations with an amplitude $(\Sigma_1, U_1, v_{x,1}, v_{y,1}, B_{x,1}, B_{y,1}) = 10^{-4}(1, 108, -6.16, 1, 1, 6)$ are initially imposed.

Fig. 5.— Evolution of maximum surface density for nonlinear MJJs. $Q = 1.5$, $n_J = 5$, and $\beta = 1$ are adopted, with initial white noise perturbations of amplitude $10^{-3}\Sigma_0$. Since $q = 0.1$ gives almost an exponential growth of perturbations, its evolution is not much different from the $q = 0$ case, causing overdense regions to collapse within $\sim 2 t_{\text{orb}}$. When $\gamma \gtrsim 1.6$, thermal pressure can support the collapsed regions and form bound objects.

Fig. 6.— An example of MJJs with $Q = 1.5$, $n_J = 5$, $q = 0.1$, $\beta = 1$, and $\gamma = 2$. Snapshots at $t = 2$ (*left*) and 4 (*right*) orbits show surface density in logarithmic grey scale, perturbed velocity vectors, and magnetic field lines. The arrow above each frame measures the amplitudes of velocity vectors, and the numbers in the grey scale bars correspond to $\log \Sigma/\Sigma_0$.

Fig. 7.— Time evolution of maximum surface density in pure hydrodynamic simulations for models H01 to H13.

Fig. 8.— Comparative snapshots of density structure in logarithmic grey scale for model H09 with $Q = 1.0$ (left) and for model H13 with $Q = 1.4$ (right). The numbers in the grey scale bars correspond to $\log \Sigma/\Sigma_0$.

Fig. 9.— Effects on the evolution of hydrodynamic simulations of (a) adiabatic index γ , (b) simulation box size (equal to $\lambda_J n_J$), and (c) numerical resolution. All models have $\epsilon_0 = 10^{-2}$ initially.

Fig. 10.— Time evolution of maximum surface density in MHD simulations with $\beta = 10$ (models M01 to M14).

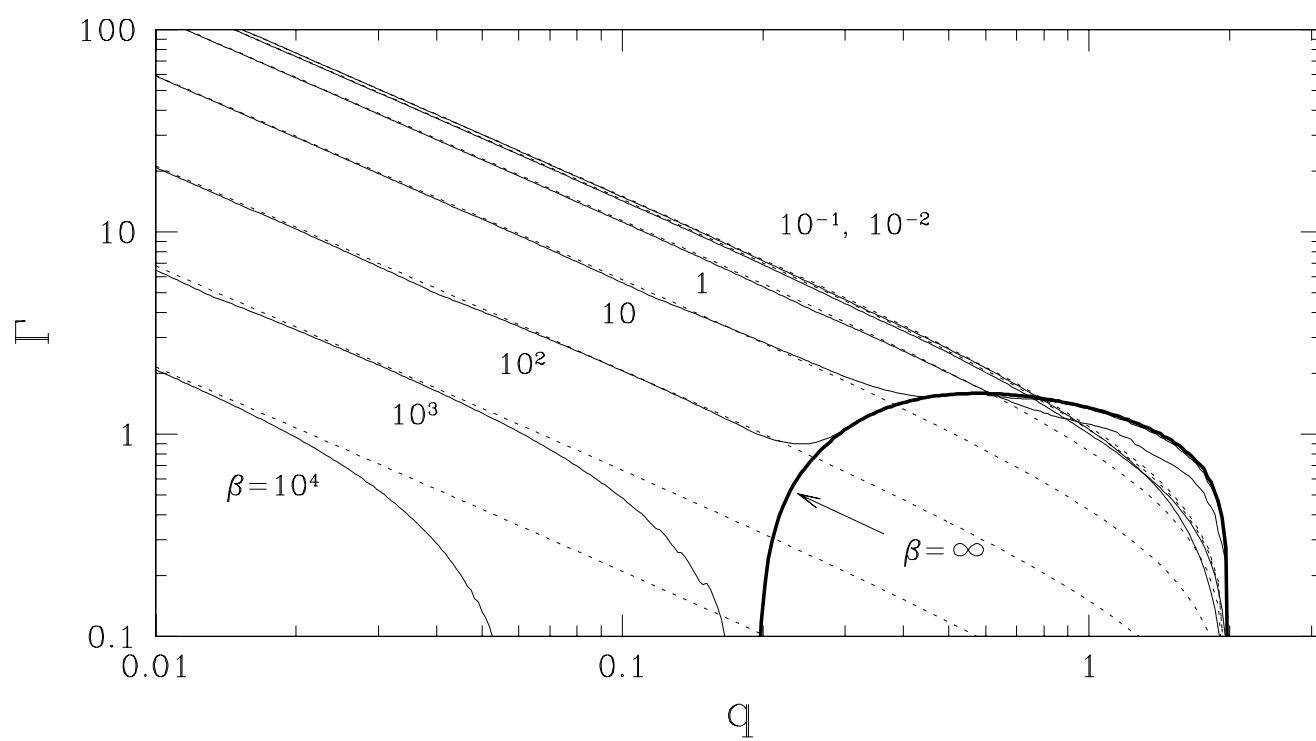
Fig. 11.— Time evolution of maximum surface density in MHD simulations with $\beta = 1$ (models M15 to M26).

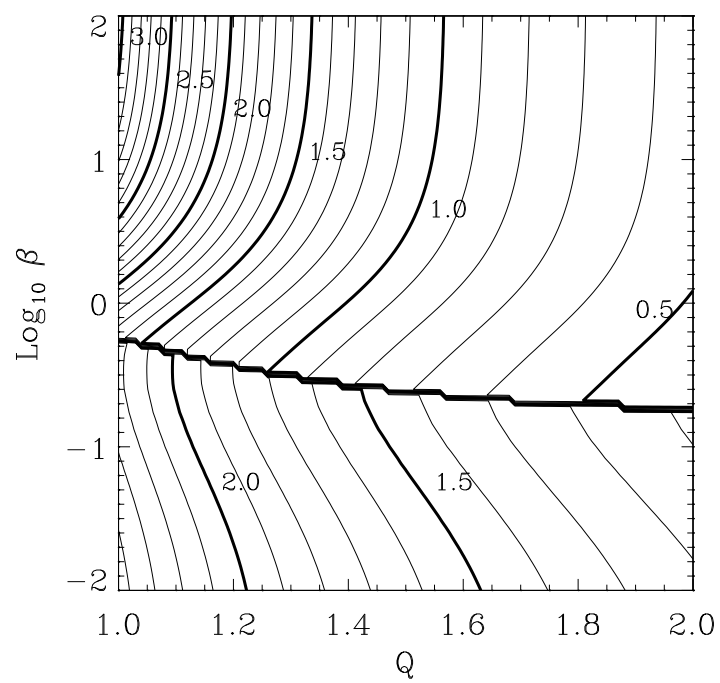
Fig. 12.— Comparative evolution of magnetized disks with different Q but with the same magnetization of $\beta = 10$. Left (for model M10 with $Q = 1.2$) and right (for model M13 with $Q = 1.5$) columns show density structures in logarithmic grey scale with overlaid magnetic field lines. The numbers in the grey scale bars correspond to $\log \Sigma/\Sigma_0$.

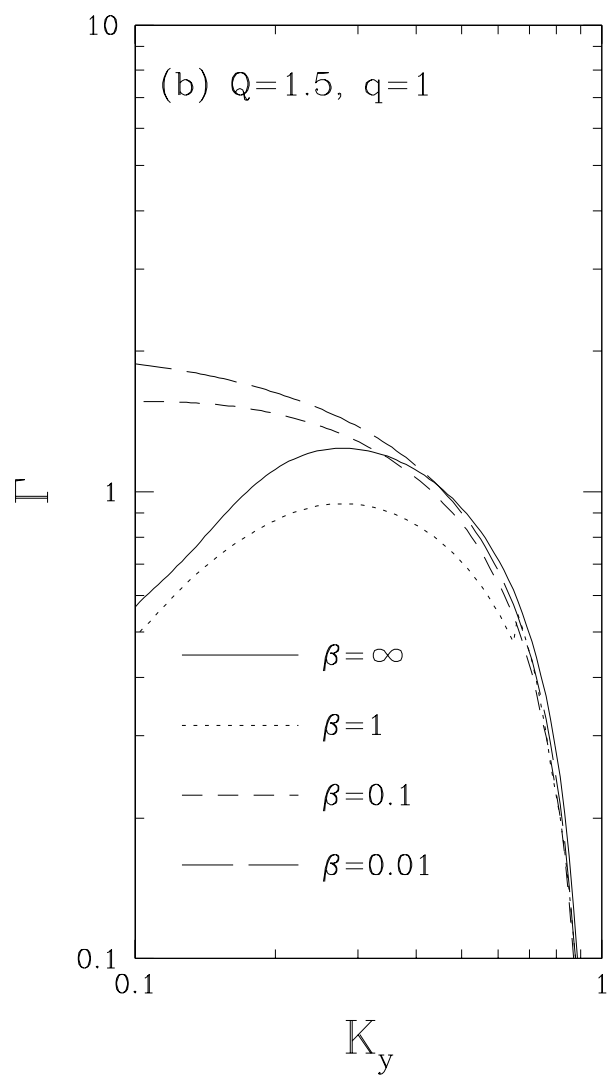
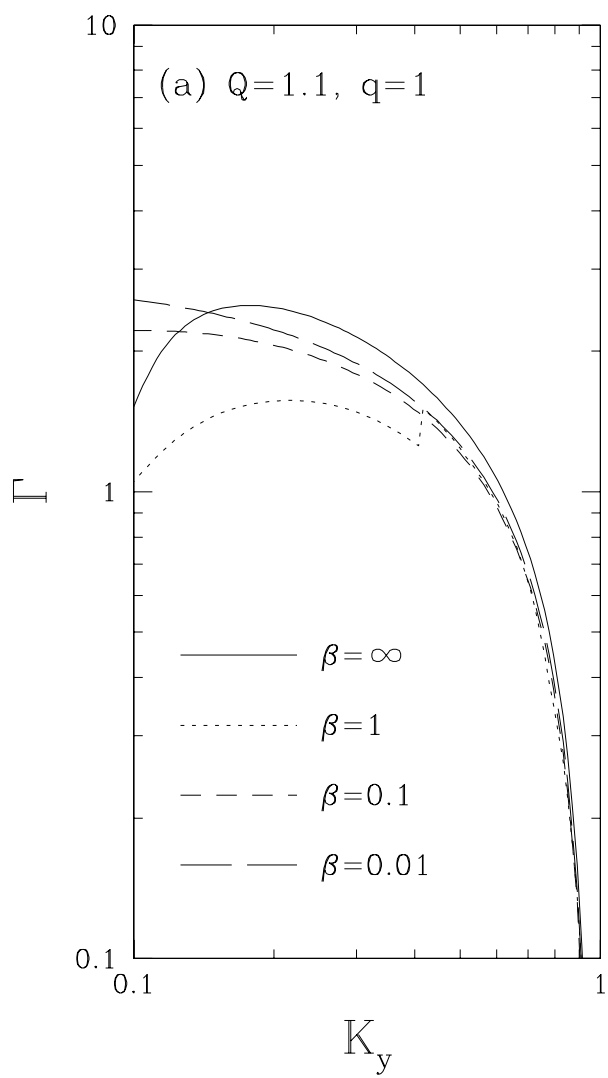
Fig. 13.— Comparative evolution of magnetized disks with different Q but with the same magnetization of $\beta = 1$. Left (for model M23 with $Q = 1.1$) and right (for model M25 with $Q = 1.3$) columns show density structures in logarithmic grey scale with overlaid magnetic field lines. The numbers in the grey scale bars correspond to $\log \Sigma/\Sigma_0$.

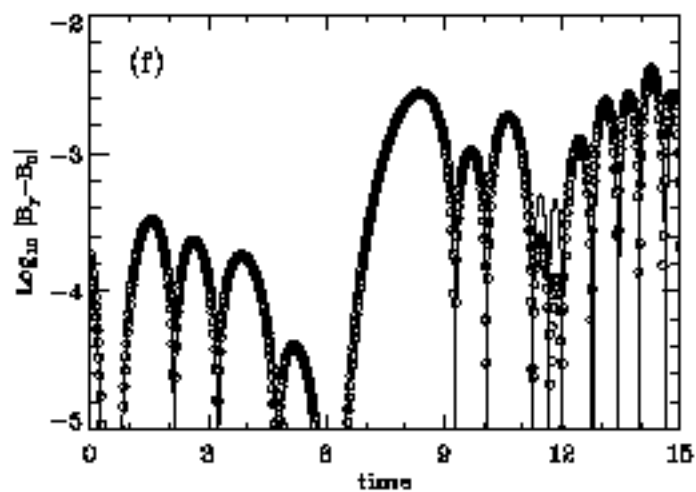
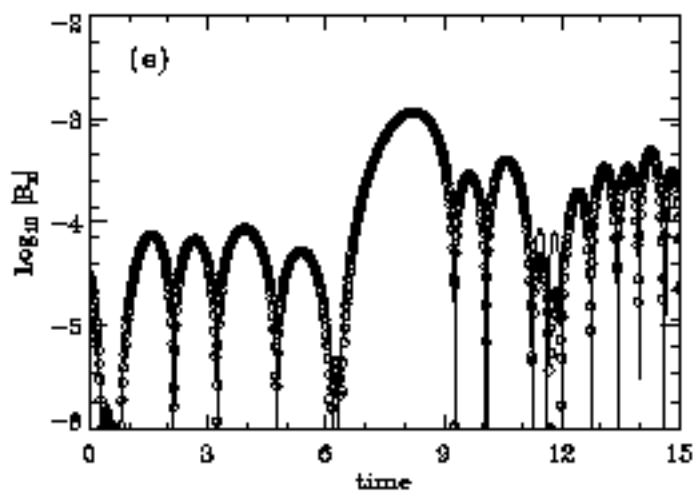
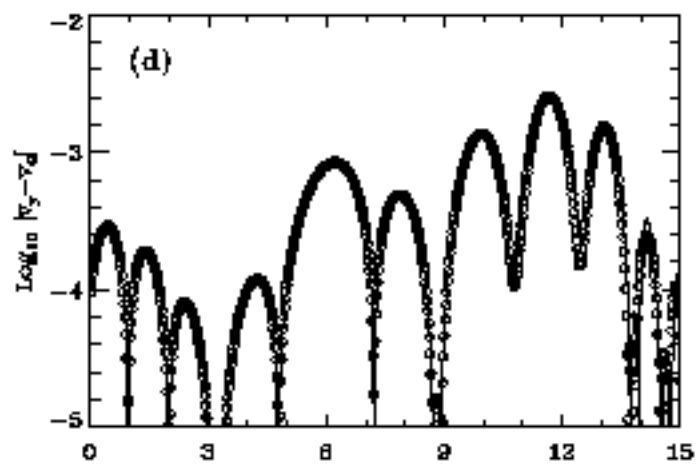
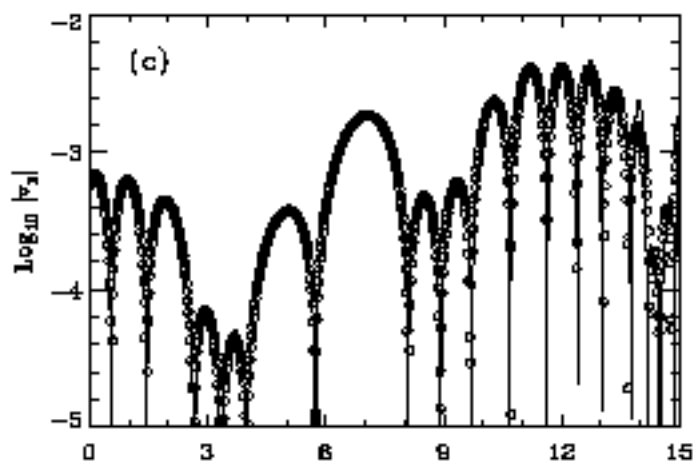
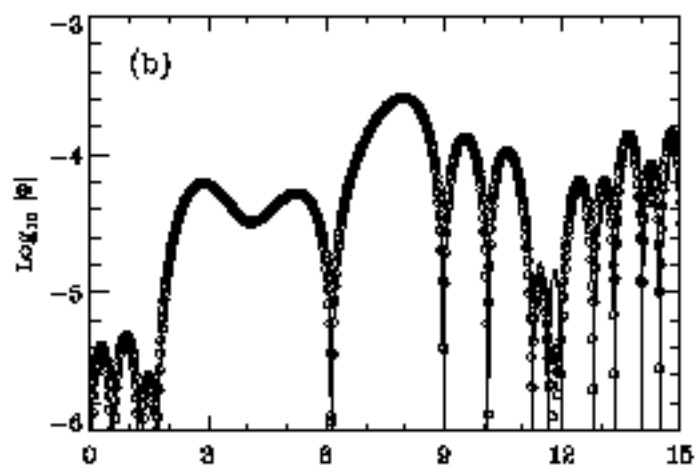
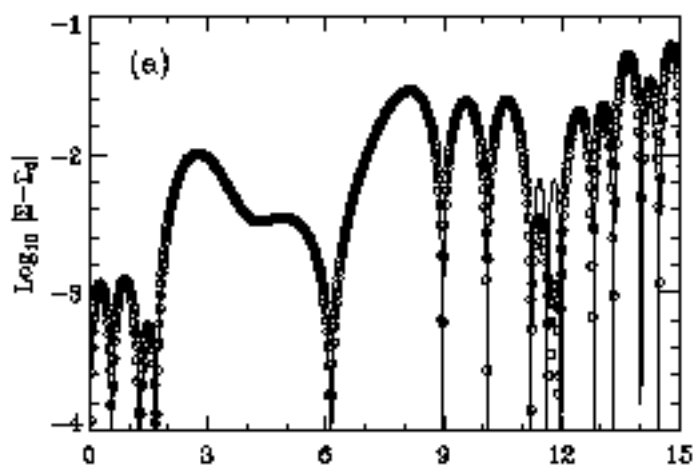
Fig. 14.— Effects on the evolution of MHD simulations with $\beta = 1$ of (a) adiabatic index γ , (b) simulation box size (given by $L = \lambda_J n_J$), and (c) the initial power spectrum of perturbations.

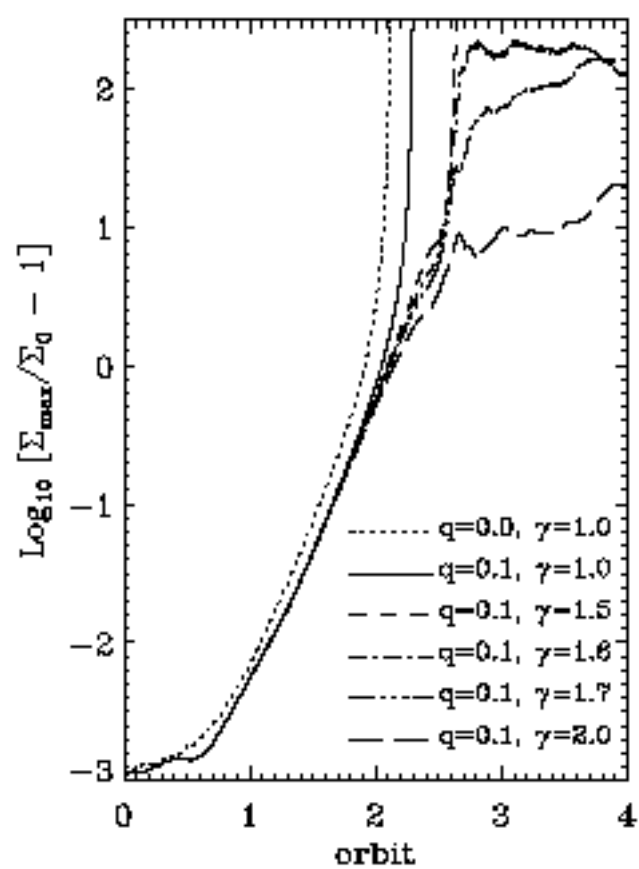
Fig. 15.— Examples of three different kinds of the secondary instabilities. The numbers in the grey scale bars correspond to $\log \Sigma/\Sigma_0$. Left: Filaments formed by MSAs experience parallel fragmentation to form gravitationally bound structures in model M05. Various symbols identify and follow each clump. Center: Collisions of nonlinear wavelets produce a high-density filament that collapses in Model M07. Boxes in the first frame highlights the portions of the wavelets that are about to undergo a collision. Circled in the last frame is the region where a bound clump forms. Right: Rejuvenated swing amplification produces a filament that subsequently collapses, in Model M23. The secondary-MSA wavefronts are represented by dotted lines. For details, see text.





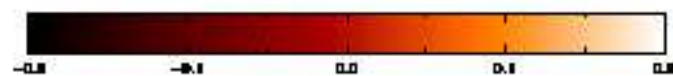
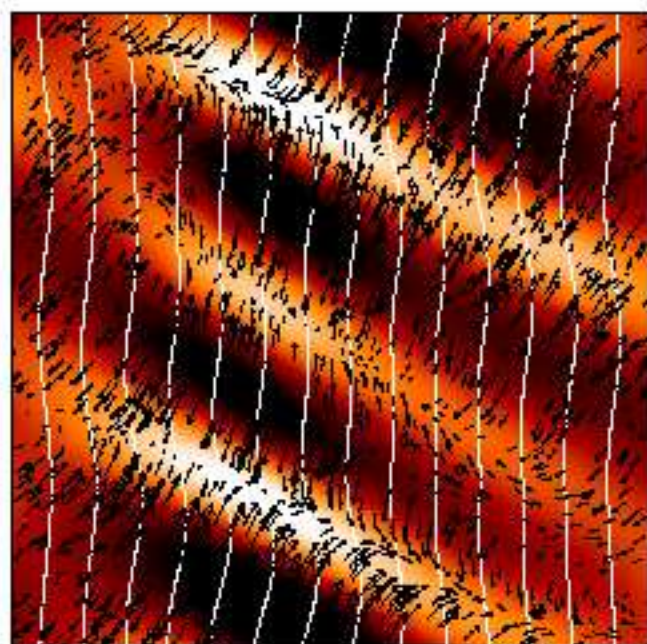






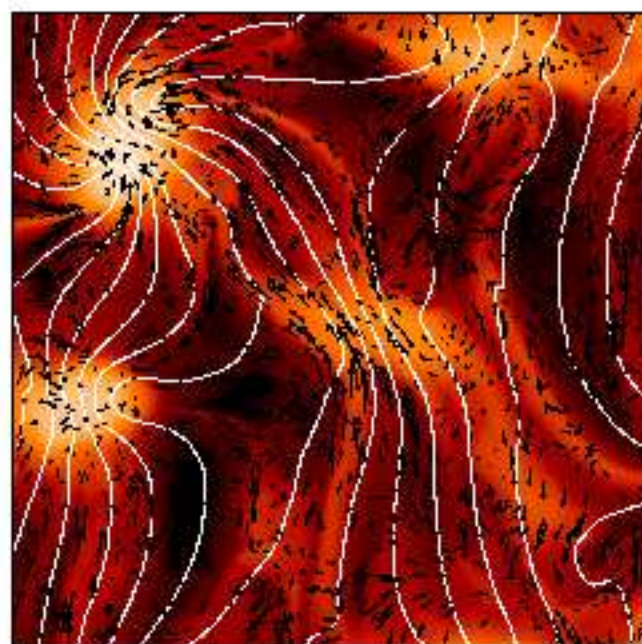
$t = 2$ orbits

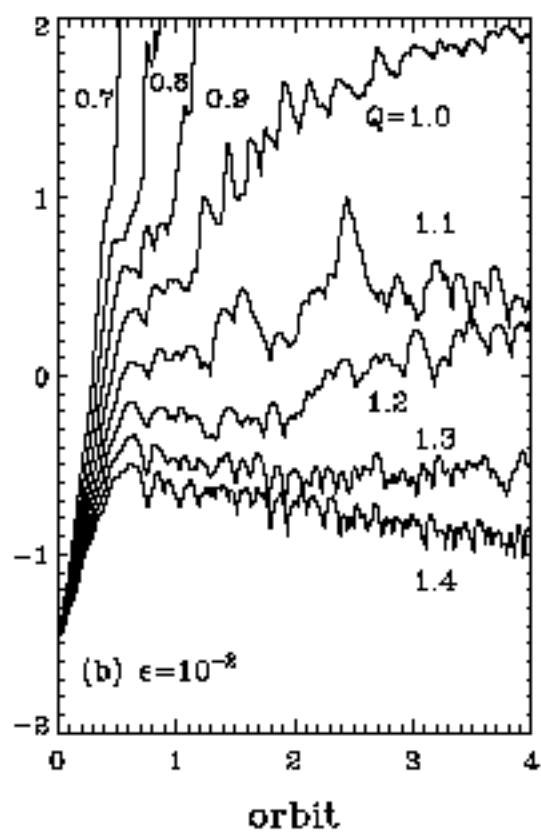
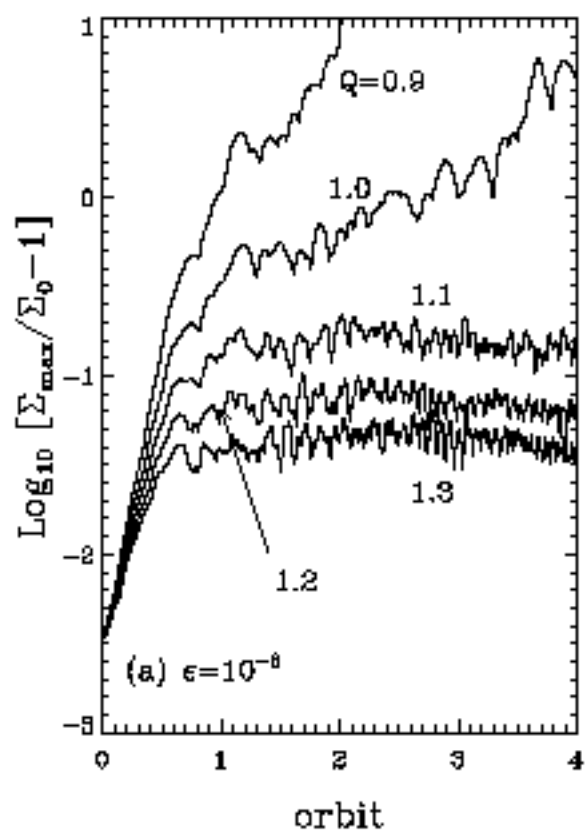
$0.03L_0 \rightarrow$



$t = 4$ orbits

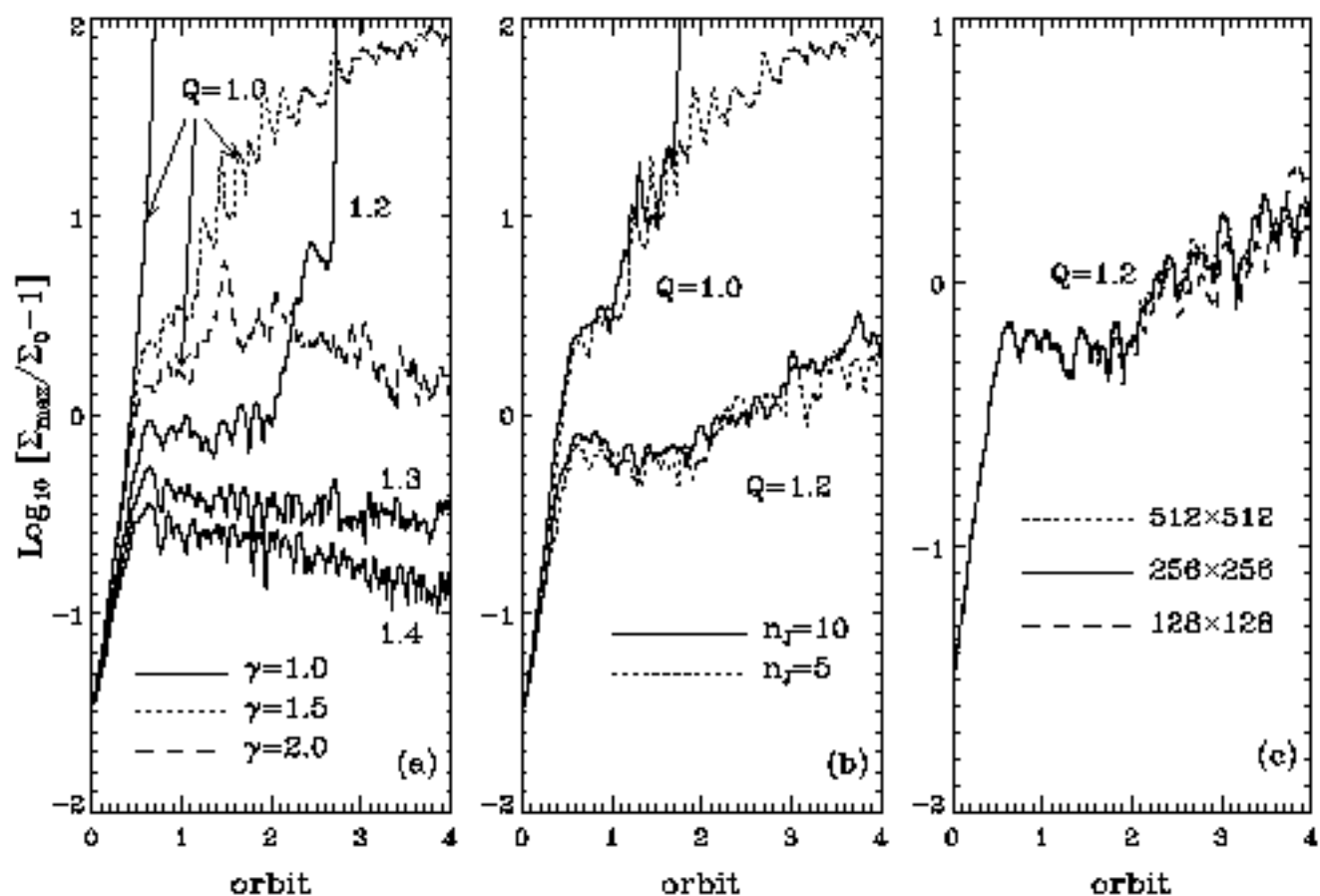
$0.8L_0 \rightarrow$

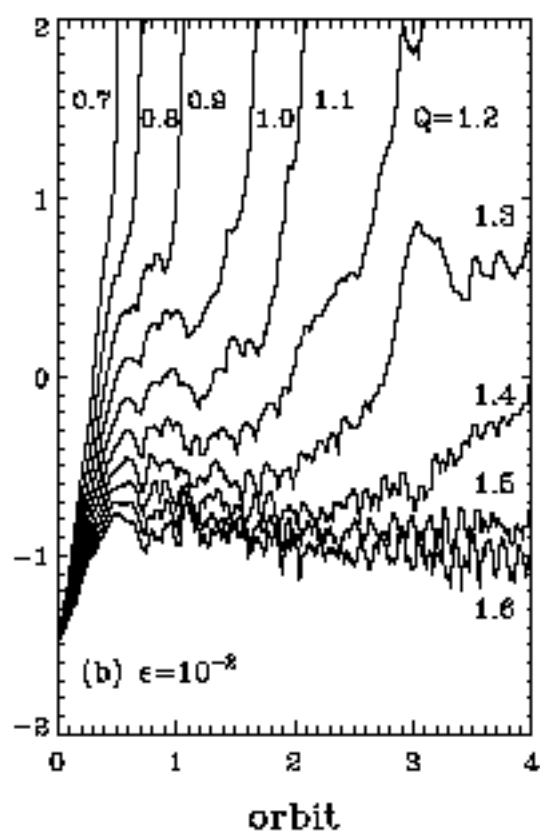
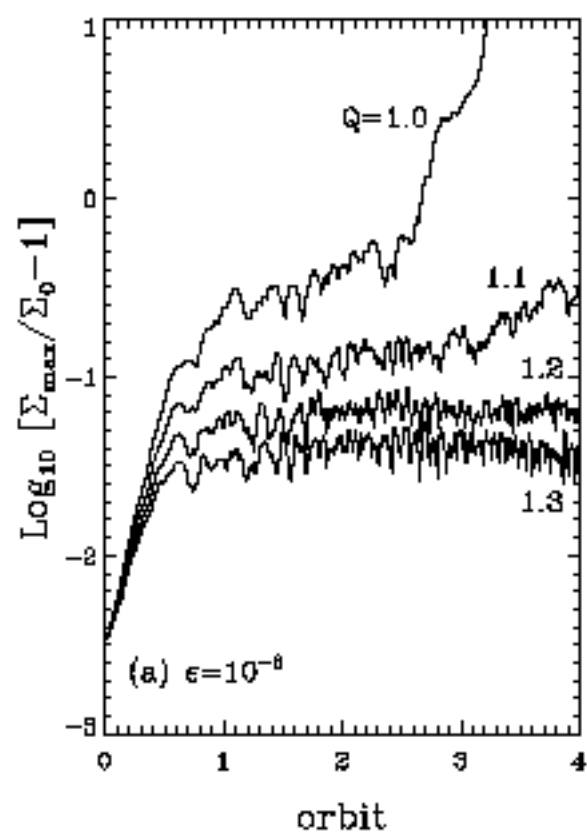


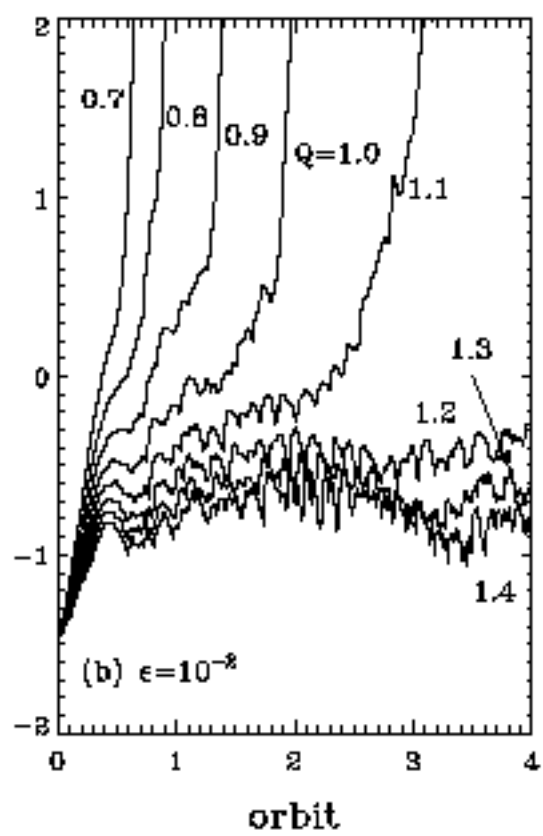
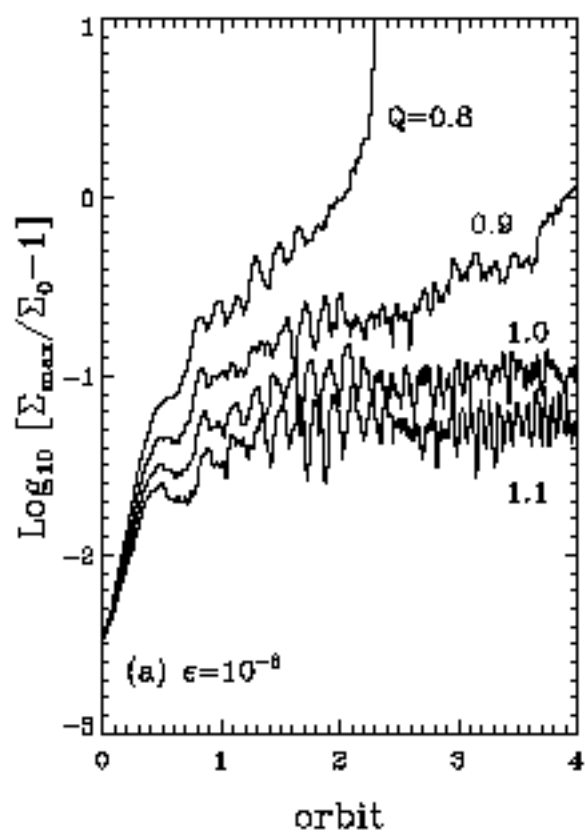


This figure "fig8.jpg" is available in "jpg" format from:

<http://arxiv.org/ps/astro-ph/0105375v1>





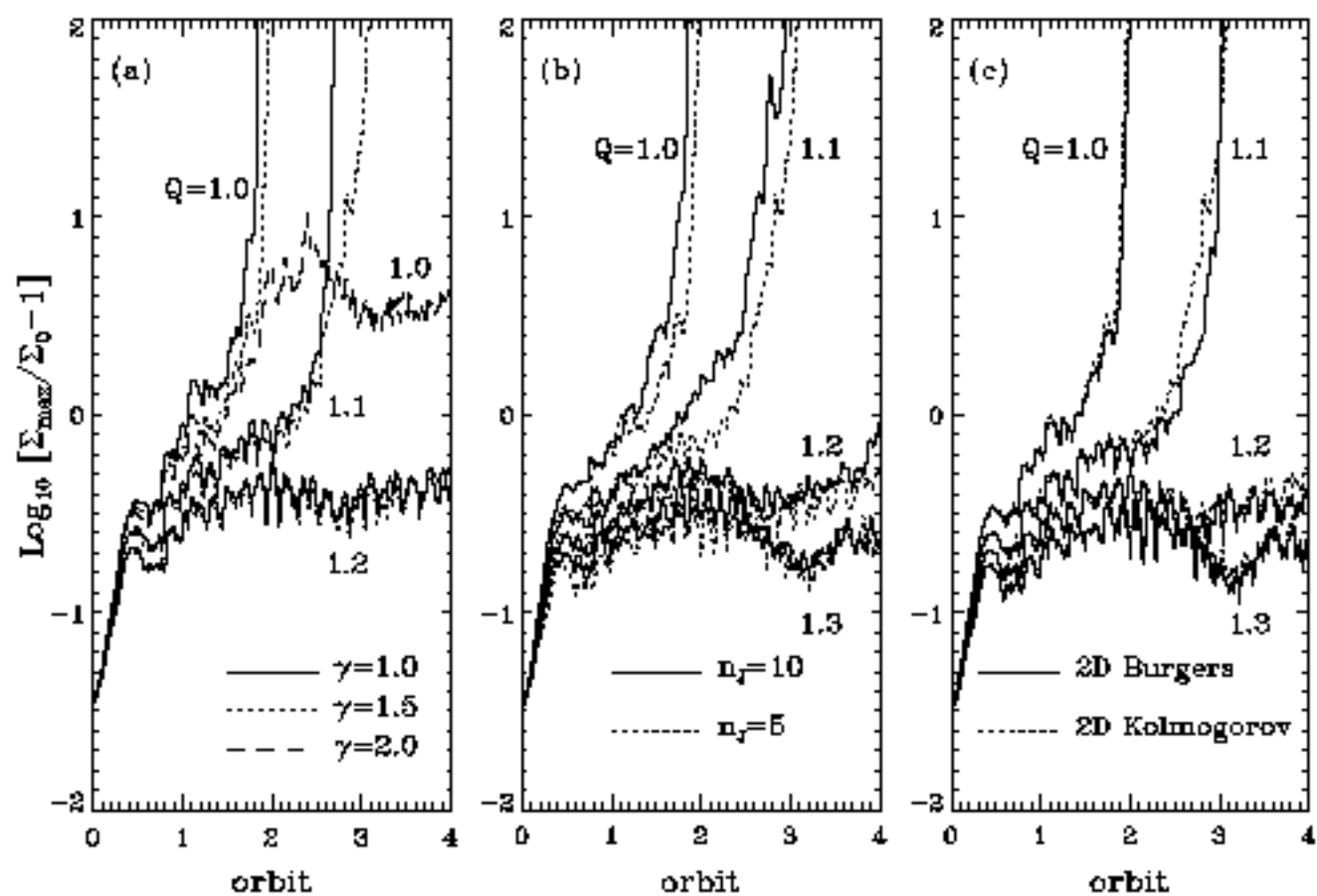


This figure "fig12.jpg" is available in "jpg" format from:

<http://arxiv.org/ps/astro-ph/0105375v1>

This figure "fig13.jpg" is available in "jpg" format from:

<http://arxiv.org/ps/astro-ph/0105375v1>



This figure "fig15.jpg" is available in "jpg" format from:

<http://arxiv.org/ps/astro-ph/0105375v1>